

CHANGING PHASES OF ALIEN WORLDS: PROBING ATMOSPHERES OF *KEPLER* PLANETS WITH HIGH-PRECISION PHOTOMETRY

LISA J. ESTEVES¹, ERNST J. W. DE MOOIJ¹ & RAY JAYAWARDHANA²

Draft version April 7, 2019

ABSTRACT

We present a comprehensive analysis of planetary phase variations, including possible planetary light offsets, using eighteen quarters of data from the *Kepler* space telescope. After correcting for systematics, we found fourteen systems with significant detections in each of the phase curve components: planet's phase function, secondary eclipse, Doppler boosting and ellipsoidal variations. We model the full phase curve simultaneously, including primary and secondary transits, and derive albedos, day- and night-side temperatures and planet masses. Most planets manifest low geometric albedos (<0.25), except for Kepler-10b, Kepler-91b and KOI-13b. We find that KOI-13b, with a small eccentricity of $6.4_{-1.6}^{+1.2} \times 10^{-4}$, is the only planet for which an eccentric orbit is favored. We detect a third harmonic for KOI-13b reported in Esteves et al. (2013): both could be due to their spin-orbit misalignments. We also performed a bootstrap analysis of each of our targets, and conclude that the photometric variations of Kepler-43b are not of planetary origin but instead a result of stellar variability and/or residual systematics. For seven planets, we find that the planetary light peak is offset from the sub-stellar point: of those, the hottest two (Kepler-76b and HAT-P-7b) exhibit shifts eastward or to the evening-side, while the cooler five (Kepler-7b, Kepler-8b, Kepler-12b, Kepler-41b and Kepler-43b) peak westward or on the morning-side. Our findings dramatically increase the number of *Kepler* planets with detected planetary light offsets, and provide the first evidence in the *Kepler* data for a correlation between the peak offset direction and the planet's temperature. Such a correlation could arise if thermal emission dominates light from hotter planets that harbor hot spots shifted to the east, as theoretically predicted, while reflected light dominates cooler planets with clouds westward of the substellar point (i.e. on the morning-side).

1. INTRODUCTION

The *Kepler Space Telescope* monitored over $\sim 150,000$ stars for nearly four years. Even though the main goal of the *Kepler* mission was to find planets using the transit method, the high precision, long baseline and continuous nature of its observations make the resulting photometry ideal for characterizing exoplanets through studies of their phase variations.

From transit measurements, it is possible to derive both the planet's orbital parameters (period, scaled semi-major axis and impact parameter) as well as the planet-to-star radius ratio. Meanwhile, the out-of-transit light curve, known as the phase curve, can yield constraints on the planetary atmosphere (e.g. albedo, brightness temperature) and the planet's mass.

A planet's phase curve is a composite of brightness variations caused by three independent phenomena: ellipsoidal variations stemming from changes in the starlight due to tides raised by the planet, Doppler boosting resulting from the reflex motion of the star, and a combination of reflected light and thermal emission from the planet. The secondary eclipse, when the planet passes behind the star, provides additional constraints on the light from the planet.

In recent years, several groups have presented light curve data from *Kepler* for a few individual planets (e.g. Welsh et al. 2010; Barclay et al. 2012; Shporer et al. 2011) and for small samples of planets (Esteves et al. 2013; Angerhausen et al. 2014; hereafter E13 and A14 respectively). With the exception of two ultra-short-period Earth-sized planets, Kepler-10b (Batalha et al. 2011) and Kepler-78b (Sanchis-Ojeda et al. 2013), all of these studies focus on hot Jupiters.

Since *Kepler* observes in a single broad optical band, it is not possible to disentangle the individual contributions from reflected light and thermal emission. The *Spitzer Space Telescope*, on the other hand, primarily probes the thermal emission from hot Jupiters at infrared wavelengths. For a number of planets, *Spitzer* observations have provided direct measurements of the day-night contrasts, due to temperature differences between the two hemispheres of these presumably tidally-locked worlds, and have shown that often the hottest spot in the planet's atmosphere is offset from the sub-stellar point (e.g. Knutson et al. 2007).

Demory et al. (2013) have shown, using *Kepler* phase curve observations and *Spitzer* secondary eclipse measurements of Kepler-7b, that a planet's brightness can be dominated by reflected light and that the albedo can vary between the morning and evening sides of the planet. They attribute this to inhomogeneous reflective clouds, whose properties change as a function of longitude, influenced by the planet's wind and thermal patterns.

Here we present the results of our transit and phase

estes@astro.utoronto.ca
demooij@astro.utoronto.ca
rayjay@yorku.ca

¹ Astronomy & Astrophysics, University of Toronto, 50 St. George Street, Toronto, Ontario M5S 3H4, Canada

² Physics & Astronomy, York University, Toronto, Ontario L3T 3R1, Canada

curve analysis, with the inclusion of a phase function offset, for 14 planets (Kepler-5b, Kepler-6b, Kepler-7b, Kepler-8b, Kepler-10b, Kepler-12b, Kepler-41b, Kepler-43b, Kepler-76b, Kepler-91b, Kepler-412b, KOI-13b, TrES-2b and HAT-P-7b) using all 18 quarters of *Kepler*'s long-cadence and short-cadence data. In Section 2 we present the dataset and our analysis method, while in Section 3 we present our model to fit the data. The results are presented and discussed in Section 4, and finally we outline our conclusions in Section 5.

2. DATA REDUCTION

After correcting for systematics (see Section 2.1), we visually inspected the phase-folded light curve of all publicly released *Kepler* planets and planet candidates with periods < 5 days. Of these we found 13 planets (Kepler-5b, Kepler-6b, Kepler-7b, Kepler-8b, Kepler-10b, Kepler-12b, Kepler-41b, Kepler-76b, Kepler-91b, Kepler-412b, KOI-13b, TrES-2b and HAT-P-7b) that, between quarters, consistently exhibited a planetary phase curve signal without requiring stellar variability removal and had significant detections in each of the phase curve components (see Section 3).

Both Kepler-17b and Kepler-43b show apparent phase curves, but the variations are not coherent between the first and the second halves of the data. Star spot activity on Kepler-17 and Kepler-43, resulting in stellar variability with 2% and 0.5% amplitudes respectively, is the most likely explanation. We chose to include Kepler-43b in our sample, but exclude Kepler-17b because of its high level of variability.

2.1. Removal of Systematics

TABLE 1
Kepler QUARTERS OF DATA USED IN ANALYSIS

System	Quarters																	
	0	1	2	3	4	5	6	7	8	9	10	11	12	13	14	15	16	17
Kepler-5	l	l	s	s	s	s	s	s	s	s	s	s	s	l	l	l	l	l
Kepler-6	l	l	s	s	s	s	s	l	s	s	s	s	l	l	l	l	l	l
Kepler-7	l	l	l	s	s	s	s	s	l	l	l	l	l	l	l	l	l	l
Kepler-8	l	l	s	s	s	s	s	l	s	s	s	s	s	l	l	l	l	l
Kepler-10	l	l	s	s	s	s	s	s	s	s	s	s	s	s	s	s	s	s
Kepler-12	l	l	s	s	s	s	s	s	s	s	s	l	l	l	l	l	l	l
Kepler-41	l	l	l	s	s	s	l	l	l	l	l	l	l	l	l	l	l	l
Kepler-43	l	l	s	s	s	s	l	s	s	s	s	s	s	s	s	l	l	l
Kepler-76	l	l	l	l	l	l	l	l	l	l	l	l	l	l	l	l	l	l
Kepler-91	l	l	l	l	l	l	l	l	l	l	l	l	l	l	l	l	l	l
Kepler-412	l	l	l	s	s	s	s	l	l	l	l	l	l	l	l	l	l	l
KOI-13	l	l	s	s	l	l	l	s	s	s	s	s	s	s	s	s	s	s
TrES-2	s	s	s	s	s	s	s	s	s	s	s	s	s	s	s	s	s	s
HAT-P-7	s	s	s	s	s	s	s	s	s	s	s	s	s	s	s	s	s	s

Long and short cadence quarters are denoted by ‘l’ and ‘s’, respectively, while an empty space indicates quarters with no data.

In our analysis, we used both the *Kepler* long cadence (LC) and short cadence (SC) simple aperture data (see Table 1). In the only multiplanet system, Kepler-10b, we removed the second planet’s transit. Instrumental signals were then removed by fitting cotrending basis vectors as described in E13. In order to remove quarter-to-quarter discontinuities, we normalized each quarter to its out-of-transit median. After cotrending and combining

all quarters, we removed outliers by calculating a running median and standard deviation of 21 measurements around each point and rejecting measurements that differed by more than 5σ . For each planet, the raw *Kepler* simple aperture photometry, the cotrended light curve and the cotrended out-of-transit light curve after outlier removal can be found in the Appendix (Figures 1-7).

2.2. Companion Stars

TABLE 2
DETECTED STELLAR COMPANIONS AROUND PLANET HOST STARS

Host Star	Host Star Kep Mag ^a	Comp. Dist (")	Comp. Est. Kep Mag	Comp. Est. Flux %
Kepler-5	13.369	0.9 ^b	18.7	$< 0.1\%$
		3.39 ^b	19.8	$< 0.1\%$
		4.94 ^b	20.3	$< 0.1\%$
Kepler-6	13.303	4.01 ^b	17.3	$< 0.1\%$
Kepler-7	12.885	1.9 ^b	16.9	$< 0.1\%$
Kepler-8	13.563	3.04 ^{b,c}	22.1	$< 0.1\%$
		3.74 ^{b,c}	20.5	$< 0.1\%$
Kepler-10	10.961	... ^{b,d}
Kepler-12	13.438	5.04 ^{b,e}	22.2	$< 0.1\%$
Kepler-41	14.465	... ^f
Kepler-43	13.958	... ^g
Kepler-76	13.308	... ^g
Kepler-91	12.495	... ^h
Kepler-412	14.309	... ^g
KOI-13	9.958	1.12 ⁱ	...	48%
TrES-2	11.338	1.09 ^{j,k,l}	...	$< 0.1\%$
HAT-P-7	10.463	3.8 ^{k,m}	...	$< 0.1\%$
		3.9 ^{k,l,m}	...	$< 0.1\%$

^a From Kepler Input Catalog.

^b From Adams et al. (2012).

^c From Jenkins et al. (2010).

^d From Batalha et al. (2011).

^e From Fortney et al. (2011).

^f No high resolution images available. However,

Quintana et al. (2013) test

dilution scenarios and do not

find a significant third light

contribution.

^g No data is available.

^h From Lillo-Box et al.

(2013).

ⁱ From Shporer et al. (2014).

^j From Daemgen et al.

(2009).

^k From Bergfors et al. (2013).

^l From Faedi et al. (2013).

^m From Narita et al. (2012).

Kepler's large pixel size, with a width of $3.98''$, allows for the possibility of dilution from a background or foreground star or a nearby stellar companion. In the literature we found that several of our 14 systems have one or more nearby stellar companions (see Table 2). However, only KOI-13 is significantly diluted by its companion. For KOI-13, studies find a large range of dilutions: 38-48% (Adams et al. 2012; Szabó et al. 2011; Shporer et al. 2014). In our analysis, we adopt the Shporer et al. (2014) value of 48%, corresponding to a dilution factor of 1.913 ± 0.019 . We also account for the quarter-to-quarter third light fraction provided by the *Kepler* Input Catalog, the average of which can be found in Tables 4-7.

2.3. Stellar Variability

For each system, we inspected the periodogram (Zechmeister & Kürster 2009) of the out-of-transit light curve and found that none of the systems has significant stellar variability at periods that are close to harmonics of the planet’s period. However, for

TABLE 3
RELEVANT CONSTANTS FOR DOPPLER BOOSTING AND ELLIPSOIDAL
MODELLING

	α_d	α_1	α_2	f_1	f_2	u	y
Kepler-5b	3.44	0.0325	1.31	0.0975	0.163	0.290	0.545
Kepler-6b	3.84	0.0435	1.45	0.130	0.217	0.398	0.628
Kepler-7b	3.68	0.0382	1.37	0.111	0.190	0.344	0.582
Kepler-8b	3.51	0.0335	1.32	0.0955	0.167	0.299	0.549
Kepler-10b	3.85	0.0430	1.42	0.125	0.214	0.391	0.603
Kepler-12b	3.66	0.0378	1.37	0.113	0.189	0.341	0.580
Kepler-41b	3.85	0.0439	1.45	0.121	0.217	0.402	0.629
Kepler-43b	3.61	0.0364	1.37	0.105	0.181	0.329	0.586
Kepler-76b	3.38	0.0308	1.29	0.0726	0.150	0.273	0.532
Kepler-91b	4.66	0.0576	1.65	-0.0541	0.249	0.545	0.735
Kepler-412b	3.77	0.0415	1.42	0.109	0.205	0.379	0.613
TrES-2b	3.71	0.0392	1.37	0.112	0.195	0.354	0.580
HAT-P-7b	3.41	0.0316	1.31	0.0888	0.157	0.282	0.551
KOI-13b ^a	2.77	0.0461	1.32	0.136	0.230	0.406	0.477
KOI-13b ^b	2.27	0.0612	1.37	0.181	0.306	0.539	0.443
KOI-13b ^c	2.43	0.0698	1.46	0.206	0.348	0.624	0.476

Notes. Although α_1 , u and y are not explicitly mentioned in this paper their description and use in calculating α_2 , f_1 and f_2 can be found in Esteves et al. (2013).

Derived using stellar parameters from:

^a Shporer et al. (2014).

^b Huber et al. (2013).

^c Szabó et al. (2011).

four of the planets (Kepler-10b, Kepler-41b, Kepler-43b and Kepler-412b), when we inspect the out-of-transit periodogram we see excess variability at periods above and below harmonics of the planet’s period. To test if this was caused by uneven sampling of the light curve, we created periodograms with similarly sampled noise and found that this phenomenon was not seen. The source of this variability is most likely star spots. By phase-folding over many orbital periods this variability should result in an increase of the scatter and should not alter the shape of the phase curve. However, for Kepler-43b our bootstrap analysis has shown that variability can have a strong influence on the shape of the phase curve (see Section 4.1).

3. ANALYSIS

3.1. Transit and Phase Curve Modeling

In our analysis, we simultaneously fit the transit and phase curve, allowing for both circular and eccentric orbits. Our model is a combination of the four components: i) F_{transit} , a Mandel & Agol (2002) transit model for a quadratically limb-darkened source; ii) F_p , the planet’s phase function; iii) F_{ecl} , the secondary eclipse, when the light from the planet is blocked as it passes behind its host star; iv) F_m , a combination of Doppler boosting and ellipsoidal variations, where Doppler boosting is caused by the host star’s changing radial velocity and ellipsoidal variations resulting from tides on the star raised by the planet. Each of these components is phase (ϕ) dependent with ϕ running from 0 to 1 and mid-transit occurring at $\phi=0$. The change in brightness of the planet-star system as a function of phase can then be described by

$$\frac{\Delta F}{F} = f_0 + F_{\text{transit}}(\phi) \cdot F_m(\phi) + F_{\text{ecl}}(\phi) + F_p(\phi + \theta) \quad (1)$$

where f_0 is an arbitrary zero-point in flux and θ is the offset of the phase function’s peak from $\phi = 0.5$. The transit model includes the impact parameter of the transit (b), the ratio of the semi-major axis of the planet’s orbit to the stellar radius (a/R_*), the planet to star radius ratio (R_p/R_*) and a linear combination of limb-darkening coefficients ($2u_1 + u_2$, $u_1 - 2u_2$). While the phase curve model fits for the planet’s mass (M_p), secondary eclipse depth (F_{ecl}) and phase function amplitude and offset (A_p and θ). Our orbital period (P) was taken from the NASA Exoplanet Archive (Akeson et al. 2013) and our time of mid-transit (T_0) was determined from a simple fit to speed up our Markov Chain Monte Carlo (MCMC) analysis.

The light curves were phase-folded and binned such that 400 points spanned the orbit (i.e. a binsize of 0.0025 in phase), but with an increased sampling rate across the transit, such that it is spanned by 200 points. However, for Kepler-76b and Kepler-91b, which only have LC measurements, we fit to the unbinned light curve taking the sampling into account. This is important as sharp features in the light curve are smoothed significantly by the long exposures.

KOI-13b’s transit curve is asymmetric as a result of the planet’s motion across a stellar surface temperature gradient during transit (Szabó et al. 2011). To obtain a symmetric curve we reflected the binned transit onto itself and fitted the mean of each bin.

In our analysis we fit two phase curve models that differ only in their treatment of F_m . One model fits for M_p directly, while the other assumes a constant amplitude derived from published radial velocity (RV) measurements, if available. In addition, each model is fit with and without θ and eccentricity as free parameters. For completeness we also fit each model with and without a cosine third harmonic that we allowed to vary in amplitude (A_3) and phase (θ_3). Our motivation for the latter came from the discovery of a phase-shifted 6.7 ± 0.3 ppm third harmonic in the residual of KOI-13b’s phase curve (E13).

Five sequences of 400,000 steps were generated and the first 150,000 points were trimmed to avoid any contamination from the initial conditions. The chains were then combined after checking that they were well mixed (Gelman & Rubin 1992) and the best-fit model was chosen using the Bayesian Information Criterion (BIC, Liddle 2007).

3.2. Eccentric Orbital Parameters

In our eccentric model we fit for eccentricity (e) and the argument of periapsis (ω), but jump in $\sqrt{e} \cos \omega$ and $\sqrt{e} \sin \omega$ (e.g. Triaud et al. 2011).

For eccentric orbits, unlike for circular orbits, the true anomaly (ν) does not change linearly in time and the star-planet separation (d) is time dependent. To adjust our phase curve model to account for this, the true anomaly and the separation were calculated in a manner similar to Bonavita et al. (2012 2013), derived using the

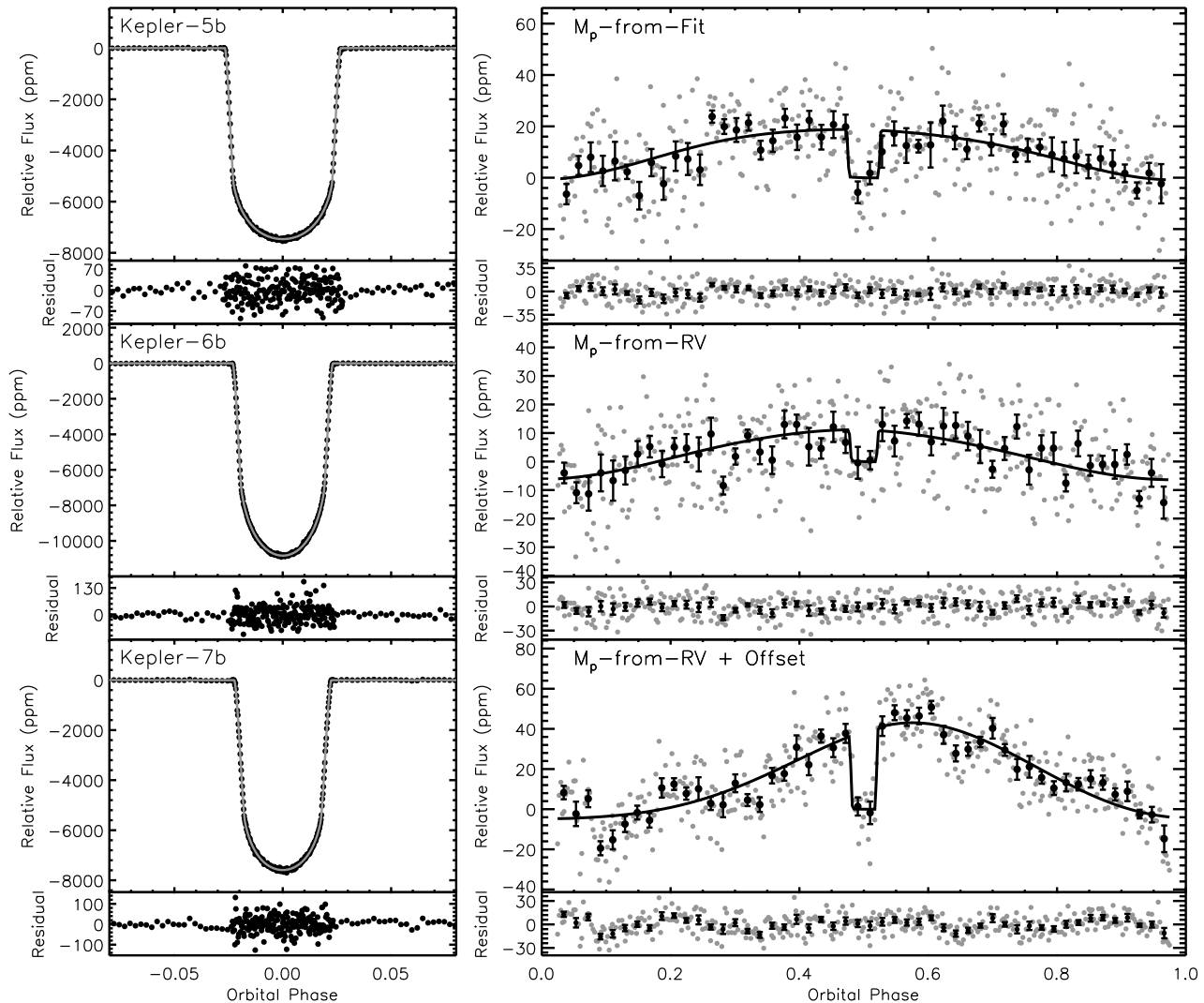


FIG. 1.— The left and right panels contain the binned and phase-folded transit light curves and phase curves, respectively. For Kepler-5b, Kepler-6b and Kepler-7b the transit data was binned to 1.36, 1.07 and 1.61 minutes, while the phase curve data (grey) was binned to 12.8, 11.6 and 17.6 minutes, respectively. Over-plotted on each is our best fit model and the phase curve data binned to four times the fitted data (black).

ephemeris formulae of Heintz (1978), as

$$E_0 = M + e \sin M + \frac{e^2}{2} \sin(2M) \quad (2)$$

$$E_{n+1} = E_n + \frac{M - E_n + e \sin E_n}{1 - e \cos E_n} \quad (3)$$

$$\nu = \frac{1}{\pi} \arctan \left\{ \sqrt{\frac{1+e}{1-e}} \tan \left(\frac{E}{2} \right) \right\} \quad (4)$$

$$d = a \frac{1 - e^2}{1 + e \cos \nu} \quad (5)$$

where M is mean anomaly, E is the eccentric anomaly and a , the semi-major axis, can be calculated from d and the planet-star separation during transit.

The projected star-planet separation (z_0) can then be calculated by

$$z_0 = \frac{d}{R_\star} \sqrt{1 - \sin^2(\nu + \omega) \sin^2 i} \quad (6)$$

where i is the orbital inclination.

Note that the mean anomaly is defined from periastron passage as

$$M = 2\pi \frac{t - T_{\text{peri}}}{P} \quad (7)$$

where T_{peri} is the time of periastron passage. This is important because the orbital phase used in our models is defined from mid-transit as

$$\phi = 2\pi \frac{t - T_{\text{mid}}}{P} \quad (8)$$

where T_{mid} is the time of mid-transit. As a result, there is a phase offset between M and ϕ . This phase offset is taken into account by requiring that $\nu + \omega$ at mid-transit be 90° . Subsequently all parameters computed from M ($\nu + \omega$, d and z_0) must be similarly offset.

In Sections 3.3- 3.4 we describe the circular phase curve models. The eccentric models can be obtained by substituting ϕ for $\nu + \omega$ and a for d .

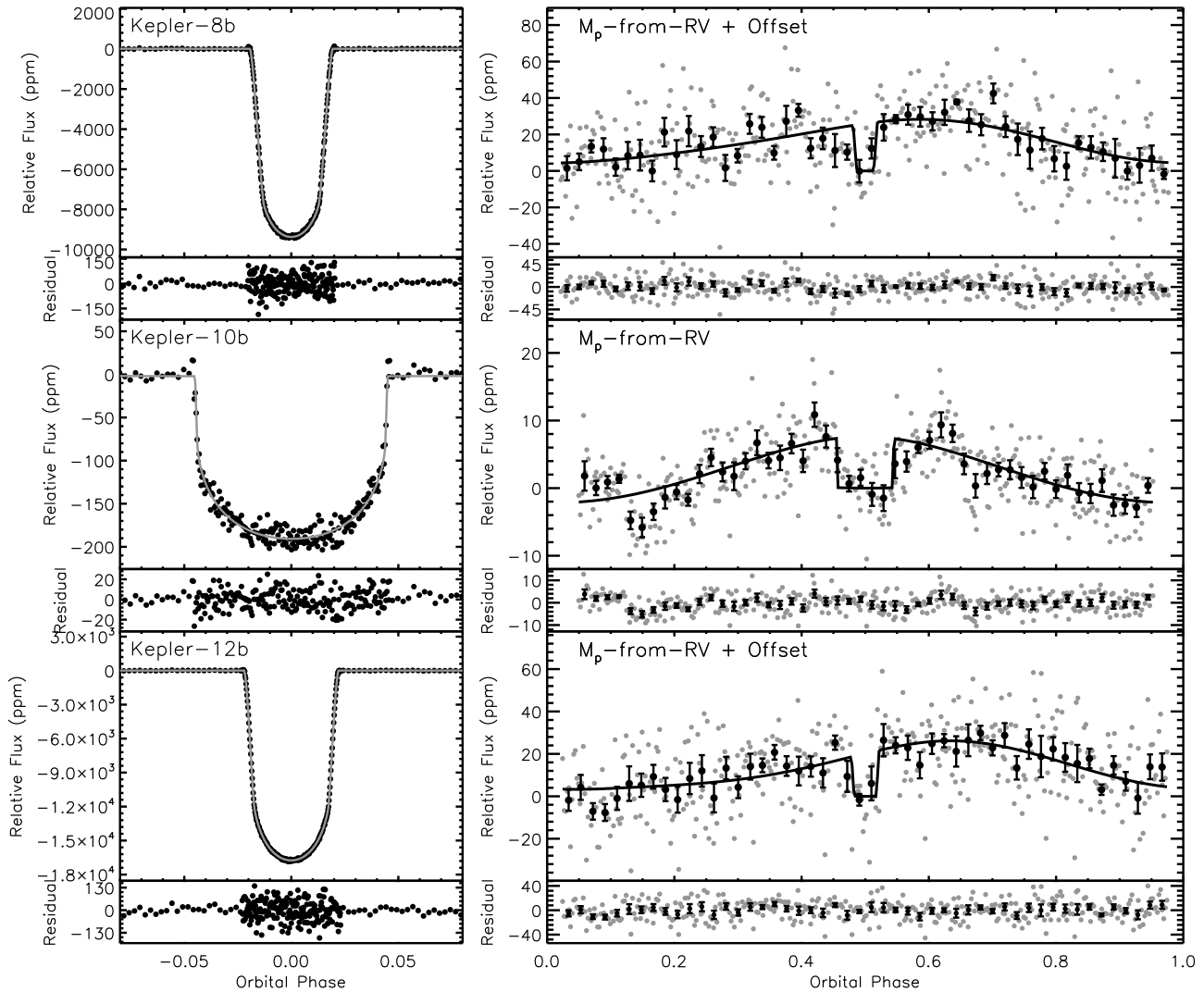


FIG. 2.— Same as Fig. 1. However, for Kepler-8b, Kepler-10b and Kepler-12b the transit was binned to 0.98, 0.55 and 1.38 minutes, while the phase curve (grey) was binned to 12.7, 3.0 and 16.0 minutes, respectively.

3.3. Secondary Eclipse and Phase Function

We model the secondary eclipse using the formalism from Mandel & Agol (2002) for a uniform source and normalize the model by R_p^2/R_*^2 . Here an eclipse model amplitude of one corresponds to a fully occulted planet while a grazing eclipse results in an amplitude less than one. The phase function is modeled as a Lambert sphere described by

$$F_p = A_p \frac{\sin z + (\pi - z) \cos z}{\pi} \quad (9)$$

where A_p is the amplitude of the phase function, R_p is the planet's radius and z is defined by

$$\cos(z) = -\sin i \cos(2\pi[\phi + \theta]) \quad (10)$$

The geometric albedo (A_g), assuming only reflected light, can then be calculated by

$$F_{\text{ecl}} = A_g \left(\frac{R_p}{a} \right)^2 \quad (11)$$

3.4. Doppler Boosting and Ellipsoidal Variations

Doppler boosting and ellipsoidal variations are two separate phenomena, both of which depend of the planet's mass (M_p) as well as other transit and stellar parameters.

Doppler boosting is a combination of a bolometric and a bandpass-dependent effect. The bolometric effect is the result of non-relativistic Doppler boosting of the stellar light in the direction of the star's radial velocity. The observed periodic brightness change is proportional to the star's radial velocity, which is a function of the planet's distance and mass. The bandpass-dependent effect is a periodic red/blue shift of the star's spectrum, which results in a periodic change of the measured brightness as parts of the star's spectrum move in and out of the observed bandpass.

Ellipsoidal variations, on the other hand, are periodic changes in observed stellar flux caused by fluctuations of the star's visible surface area as the stellar tide, created by the planet, rotates in and out of view of the observer. If there is no tidal lag, the star's visible surface area and

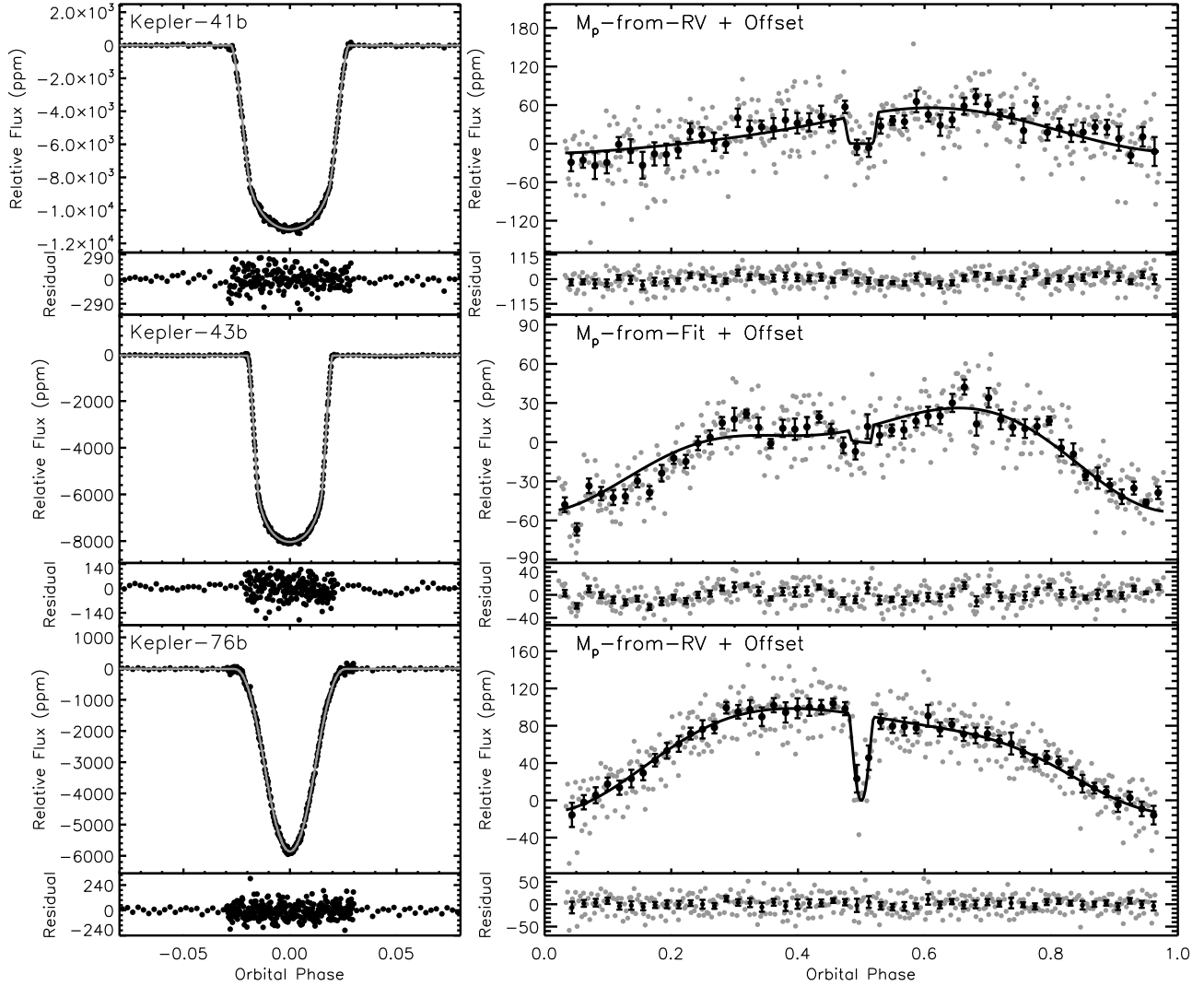


FIG. 3.— Same as Fig. 1. However, for Kepler-41b, Kepler-43b and Kepler-76b the transit was binned to 0.74, 0.89 and 0.45 minutes, while the phase curve (grey) was binned to 6.7, 10.9 and 5.6 minutes, respectively.

ellipsoidal variations are at maximum when the direction of the tidal bulge is perpendicular to the observer's line of sight, ϕ of 0.25 and 0.75, and at minimum during the transit and the secondary eclipse.

The combined Doppler and ellipsoidal contributions can be described by

$$F_m = M_p \cdot \left\{ \begin{array}{l} \left(\frac{2\pi G}{P} \right)^{1/3} \frac{\alpha_d \sin i}{c \cdot M_*^{2/3}} \left(\frac{1+e \cos \omega}{\sqrt{1-e^2}} \right) f_d \\ - \frac{\alpha_2 \sin^2 i}{M_*} f_e \end{array} \right\} \quad (12)$$

where M_* is the host star mass, G is the universal gravitational constant, c is the speed of light, α_d is the photon-weighted bandpass-integrated beaming factor and f_d and f_e are the phase dependent modulations of the Doppler boosting and ellipsoidal signals, respectively. f_d and f_e

can be described by

$$f_d = \sin(2\pi\phi) \quad (13)$$

$$f_e = \left(\frac{a}{R_*} \right)^{-3} \cos(2 \cdot 2\pi\phi) + \left(\frac{a}{R_*} \right)^{-4} f_1 \cos(2\pi\phi) + \left(\frac{a}{R_*} \right)^{-4} f_2 \cos(3 \cdot 2\pi\phi) \quad (14)$$

Here f_1 and f_2 are constants used to determine the amplitude of the higher-order ellipsoidal variations and are defined by

$$f_1 = 3\alpha_1 \frac{5 \sin^2 i - 4}{\sin i} \quad (15)$$

$$f_2 = 5\alpha_1 \sin i \quad (16)$$

The detailed description of α_d , α_1 and α_2 can be found in E13 and references therein. While their values, along

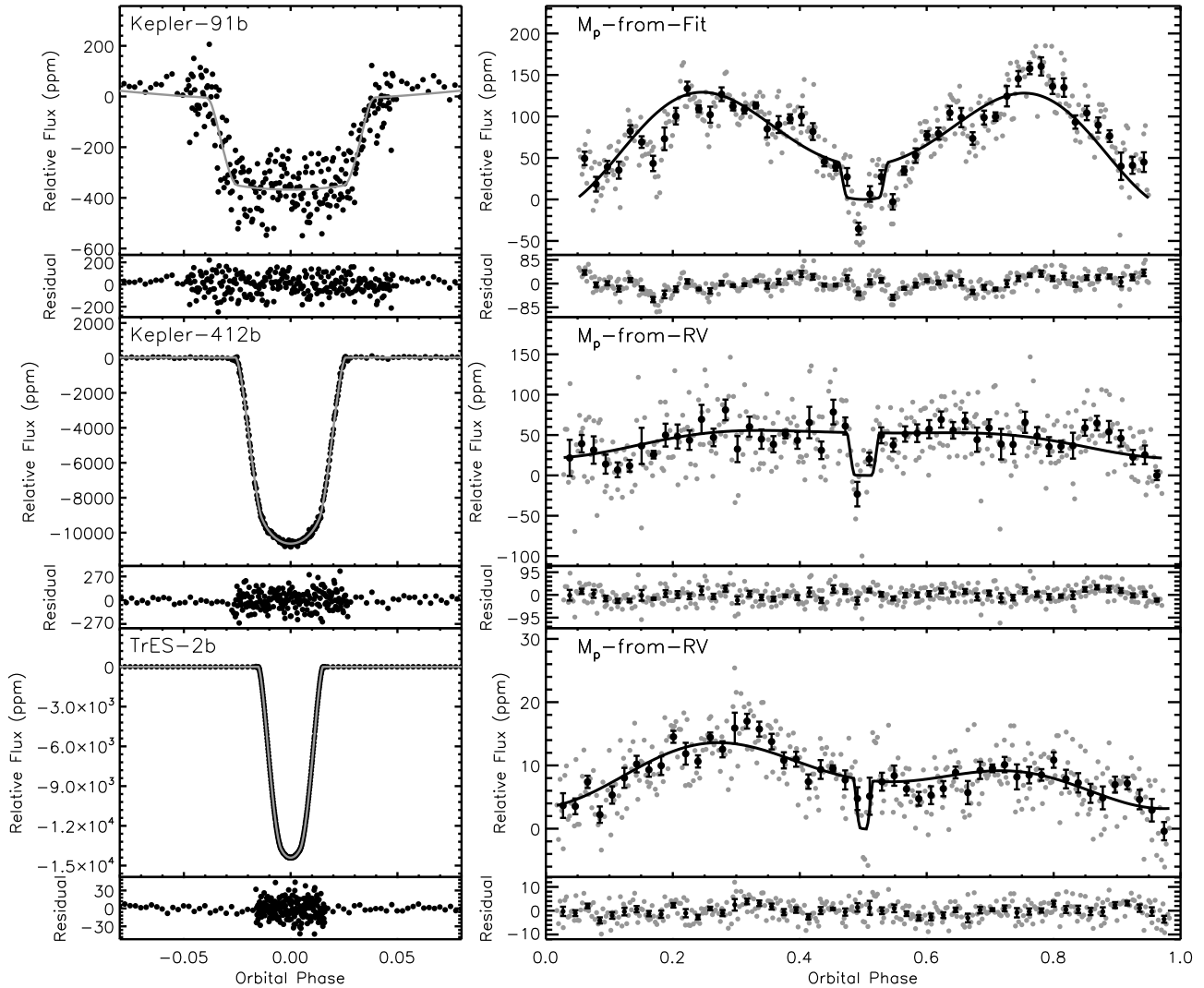


FIG. 4.— Same as Fig. 1. However, for Kepler-91b, Kepler-412b and TrES-2b the transit was binned to 3.55, 0.63 and 0.54 minutes, while the phase curve (grey) was binned to 22.5, 6.2 and 8.9 minutes, respectively.

with the values of f_1 , f_2 , can be found in Table 3.

In the RV derived model, M_p is calculated via

$$K = \left(\frac{2\pi G}{P} \right)^{1/3} \frac{M_p \sin i}{M_\star^{2/3} \sqrt{1 - e^2}} \quad (17)$$

where K is the published RV semi-amplitude (see Tables 4-7).

4. RESULTS AND DISCUSSION

Using the BIC we selected the most appropriate model for each target. The results of our best-fits can be found in Tables 4-7 and in Figs. 1-5. The errors presented for the phase function amplitude (A_p), eclipse depth (F_{ec1}) and planet mass (M_p) were derived from our bootstrap analysis (see Section 4.1). Of our targets, KOI-13b, with a small eccentricity of $6.4_{-1.6}^{+1.2} \times 10^{-4}$, is the only planet where the BIC favoured an eccentric orbit.

4.1. Robustness of Phase Curve Parameters

To assess the robustness of the phase curve parameters we performed a bootstrap, using a simple regression analysis, to measure F_{ec1} , A_p and M_p for subsets of the data. To simplify the model, the peak offset and third harmonic were fixed to the best-fit parameters from our MCMC analysis. For each fit we randomly selected half of the available individual orbits, allowing for orbits to be redrawn. However, we only selected orbits where at least 80% of the data were available, to prevent skewing from incomplete phase curves. For each planet we generated 5000 light curves and use the standard deviation of the distribution of best fit values to determine uncertainties for F_{ec1} , A_p and M_p (see Tables 4-7), but still assume a best-fit value obtained from our MCMC analysis.

For all planets we found that the uncertainty derived from the bootstrap was higher than for the MCMC, but that the median value from the bootstrap is in agreement with our best-fit MCMC values. For most planets the uncertainty was 1-3 times the MCMC values. However for the phase functions of Kepler-7b, Kepler-8b,

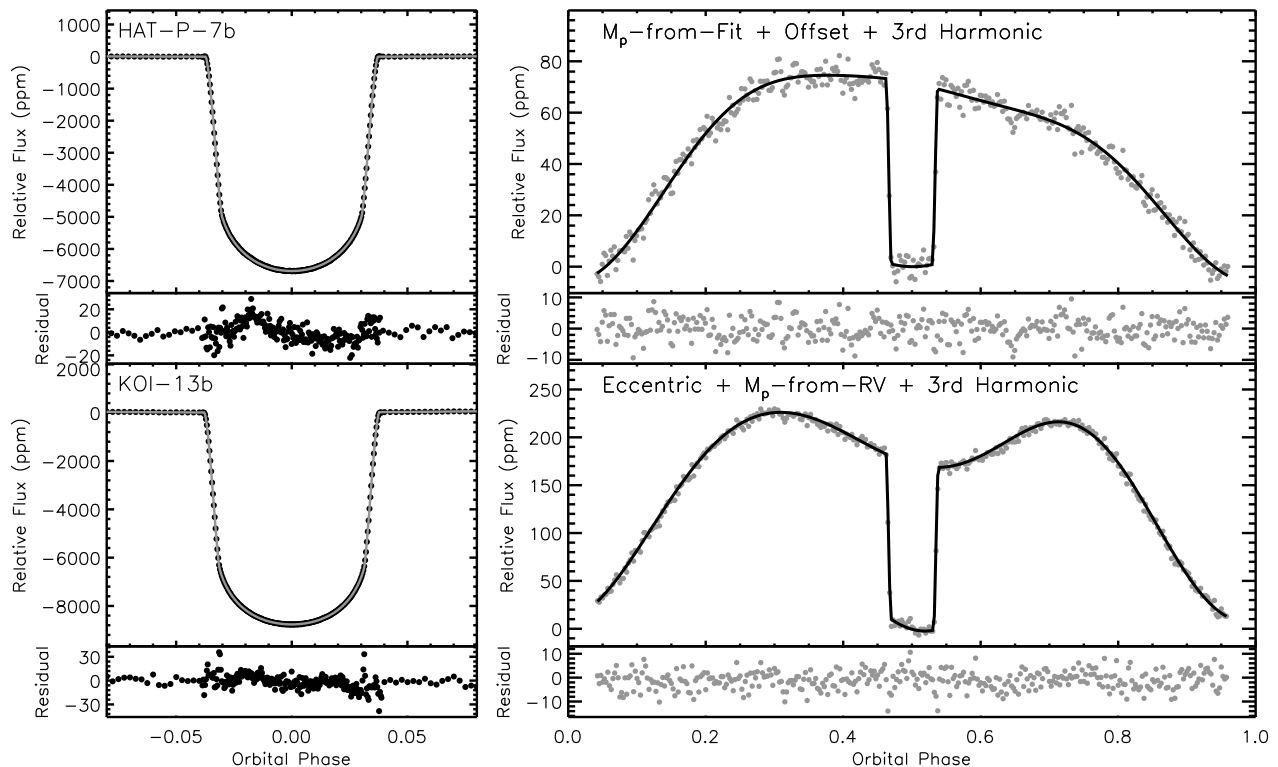


FIG. 5.— Same as Fig. 1. However, for HAT-P-7b and KOI-13b the transit data was binned to 1.18 and 0.95 minutes, while the phase curve data (grey) was binned to 7.9 and 6.4 minutes, respectively. For HAT-P-7b and KOI-13b we did not overplot the increasingly binned data as the error bars are smaller than the size of the data points.

Kepler-43b, Kepler-91b and HAT-P-7b, the bootstrap uncertainties were 8, 4, 12, 4 and 6 times higher than the MCMC, respectively. For Kepler-43b the bootstrap derived uncertainty for the eclipse depth and planet mass was also 4 and 9 times higher. It should be noted that the eclipse depth for Kepler-43b is significantly lower than the phase curve amplitude (see Table 5) and its host star appears to be variable (see Fig. 4).

For Kepler-43b we also find a phase function amplitude 7 times larger than the eclipse depth, which is only physically possible if the planet does not fully pass behind the star. This would require a highly inclined and eccentric orbit both of which are not found by our phase curve analysis and in radial velocity data from Bonomo et al. (2012). Due to the large variations in our bootstrap parameters for Kepler-43b and unphysical phase curve measurements, we conclude that it does not exhibit a planetary phase curve signal and that the variations are likely a result of residual instrumental effects or stellar variability.

These results indicate that there are residual systematic effects and/or stellar variability affecting the data, and the impact is greatest for Kepler-7b and Kepler-43b. Furthermore, the bootstrap results for Kepler-43b show that it is possible for stellar variability to mimic the shape of a phase curve and therefore additional analysis is needed to validate the planetary origin of a phase curve.

4.2. Fitted vs. Derived Planet Masses

For nine of the twelve planets with published RV measurements the BIC favoured the use of a fixed ellipsoidal and Doppler amplitude (See Tables 4-6). This indicates that, for those planets, changing the amplitude of the RV derived ellipsoidal and Doppler signal does not reduce the χ^2 enough to justify adding another parameter.

For Kepler-5b, Kepler-43b and HAT-P-7b a fitted planet mass was favoured over the RV derived value. For Kepler-5b and HAT-P-7b the fitted value was 1-2 σ lower than for RV value. This deviation from the RV mass could be a result of light curve variability as the bootstrap uncertainty for Kepler-5b and HAT-P-7b was approximately 2 and 4 times higher than the MCMC value, respectively. For Kepler-43b, we have already demonstrated that its phase curve is most likely not of planetary origin, but instead a result of light curve variability (see Section 4.1).

For the two planets with RV measurements, Kepler-91b and KOI-13b, we find that variability in their light curve results in an uncertainty 4 and 2 times larger than found by the MCMC, respectively.

4.3. KOI-13b/Kepler-13b

For KOI-13b we ran our fits using three sets of stellar parameters reported in the literature (Shporer et al. 2014; Huber et al. 2013; Szabó et al. 2011). We do this only for KOI-13b because the reported stellar parameters differ greatly from one another and more importantly because the choice of stellar parameters strongly influences our derived equilibrium temperature.

TABLE 4
STELLAR AND PLANETARY PARAMETERS

Parameter	Kepler-5b	Kepler-6b	Kepler-7b	Kepler-8b
KOI	18.01	17.01	97.01	10.01
Period (days) ^a	3.5484657±0.0000007	3.2346996±0.0000004	4.8854892±0.0000009	3.5224991±0.0000007
T_* (K)	6297±60 ^c	5647±44 ^d	5933±44 ^e	6213±150 ^g
log g (cgs)	3.96±0.10 ^c	4.236±0.011 ^d	3.98±0.1 ^e	4.174±0.026 ^g
[Fe/H]	0.04±0.06 ^c	0.34±0.04 ^d	0.11±0.03 ^e	-0.055±0.03 ^g
R_*/R_\odot	1.793 ^{+0.043} _{-0.062} ^c	1.391 ^{+0.017} _{-0.022} ^d	1.966±0.013 ^f	1.486 ^{+0.053} _{-0.062} ^g
M_*/M_\odot	1.374 ^{+0.040} _{-0.059} ^c	1.209 ^{+0.034} _{-0.038} ^d	1.359±0.031 ^f	1.213 ^{+0.067} _{-0.062} ^g
K (m/s)	227.5±2.8 ^c	80.9±2.6 ^d	42.9±3.5 ^e	68.4±12.0 ^g
M_p from RV (M_J)	2.111 ^{+0.067} _{-0.086}	0.668 ^{+0.038} _{-0.035}	0.441 ^{+0.043} _{-0.042}	0.59 ^{+0.13} _{-0.12}
Avg 3rd Light (%) ^b	3.14	2.34	1.42	2.49
Transit fit				
T_0 (BJD-2545833)	122.90144±0.00002	121.486528 ^{+0.000009} _{-0.000012}	134.27687 ^{+0.00003} _{-0.00002}	121.11931±0.00002
b	0.0968 ^{+0.035} _{-0.049}	0.141±0.022	0.5599 ^{+0.0045} _{-0.0046}	0.7191 ^{+0.0021} _{-0.0023}
R_p/R_*	0.079965 ^{+0.000087} _{-0.000071}	0.09424 ^{+0.00012} _{-0.00011}	0.08294±0.00011	0.095751 ^{+0.00019} _{-0.00023}
a/R_*	6.450 ^{+0.021} _{-0.025}	7.503±0.022	6.637±0.021	6.854 ^{+0.018} _{-0.017}
i (Degrees)	89.14 ^{+0.44} _{-0.32}	88.93 ^{+0.19} _{-0.17}	85.161 ^{+0.055} _{-0.054}	83.978 ^{+0.036} _{-0.033}
u_1	0.1741 ^{+0.0058} _{-0.0060}	0.2212 ^{+0.0059} _{-0.0060}	0.188 ^{+0.013} _{-0.014}	0.181±0.030
u_2	0.0109 ^{+0.0048} _{-0.0050}	0.0432 ^{+0.0041} _{-0.0042}	-0.0089 ^{+0.0085} _{-0.0110}	0.0096±0.024 _{-0.018}
Phase curve fit				
Best Model	M_p -from-Fit	M_p -from-RV	M_p -from-RV + Offset	M_p -from-RV + Offset
F_{ecl} (ppm)	18.6 ^{+3.7} _{-3.5}	11.1±4.0	38.7 ^{+8.1} _{-8.6}	26.0±7.6
A_p (ppm)	19.3 ^{+6.3} _{-5.3}	17.2 ^{+4.6} _{-4.0}	48±13	24±11
θ (in phase)	-0.0696±0.0052	-0.069 ^{+0.015} _{-0.016}
F_n (ppm)	-0.6 ⁺⁹ ₋₁₀	-6.2 ^{+8.0} _{-8.6}	-5±20	4±20
M_p (M_J)	0.92±0.66
Derived parameters				
R_p (R_J)	1.426 ^{+0.036} _{-0.051}	1.304 ^{+0.018} _{-0.033}	1.622±0.013	1.416 ^{+0.053} _{-0.062}
a (Au)	0.0538 ^{+0.0015} _{-0.0021}	0.04852 ^{+0.00074} _{-0.00133}	0.06067±0.00059	0.0474 ^{+0.0018} _{-0.0021}
$A_{\text{g,ecl}}$	0.121 ^{+0.025} _{-0.024}	0.070±0.026	0.248 ^{+0.055} _{-0.057}	0.133 ^{+0.041} _{-0.040}
$T_{\text{eq,max}}$ (K)	2240 ⁺³⁰ ₋₂₀	1860±20	2080±20	2140±50
$T_{\text{eq,hom}}$ (K)	1750±20	1460±10	1630±10	1680±40
$T_{\text{B,day}}$ (K)	2390 ⁺⁶⁰ ₋₇₀	2060 ⁺⁸⁰ ₋₁₀₀	2510 ⁺⁷⁰ ₋₉₀	2400±100
$T_{\text{B,night}}$ (K)	<2200(1 σ)	<1700(1 σ)	<2300(1 σ)	<2300(1 σ)
	<2400(2 σ)	<2000(2 σ)	<2500(2 σ)	<2500(2 σ)

^a From the NASA Exoplanet Archive (Akeson et al. 2013).

^b From the Kepler Input Catalog.

^c From Koch et al. (2010).

^d From Dunham et al. (2010).

^f From Demory et al. (2011).

^e From Latham et al. (2010).

^g From Jenkins et al. (2010).

This is of particular importance for KOI-13b as its blackbody peaks very close to the edge of the *Kepler* bandpass. Therefore a small increase in equilibrium temperature can lead to a significant increase in the contribution from thermal emission in the *Kepler* bandpass, while a small decrease in temperature will require a larger amount of reflected light to explain the observed secondary eclipse depth. Further discussion of KOI-13b's equilibrium temperature and albedo can be found in Section 4.8.

We note that because the ellipsoidal models depend on coefficients derived from stellar parameters (see Table 3), using values from Shporer et al. (2014) results in a BIC favoured model without a phase function offset, while using the other two sets of parameters favours a small positive offset. In addition, all three sets of stellar parameters favoured a small, but slightly different, eccentric orbit and third cosine harmonic with an amplitude of ~ 7 ppm (see Section 4.7 and Table 7).

The determination of KOI-13b's host star temperature

is complicated by the fact that it has a stellar companion at 1.12" with almost the same apparent brightness. For the rest of our discussion we adopt the results obtained using the most recent spectroscopically derived values from Shporer et al. (2014) as our best-fit values, but we note that the results for this planet strongly depend on the assumed stellar parameters.

4.4. *Kepler-76b/KOI-1658.01*

Of our targets Kepler-76b is the only planet where our fit indicates a grazing transit and therefore a partial eclipse. This results in a normalized eclipse model with an amplitude less than one (see Section 3.3), which then leads to a measured planetary flux (F_{ecl}) larger than the apparent eclipse depth. Although the eclipse does not appear much larger than the phase function (see Figure 5), compensating for the partial eclipse leads to a significant difference and therefore a large night-side flux (see Section 4.9).

TABLE 5
STELLAR AND PLANETARY PARAMETERS

Parameter	Kepler-10b	Kepler-12b	Kepler-41b	Kepler-43b
KOI	72.01	20.01	196.01	135.01
Period (days) ^a	0.837491±0.000002	4.4379629±0.0000006	1.8555577±0.0000003	3.0240949±0.0000006
T_* (K)	5627±44 ^c	5947±100 ^d	5620±140 ^e	6041±143 ^f
log g (cgs)	4.35±0.06 ^c	4.175 ^{+0.015} _{-0.011} ^d	4.47±0.12 ^e	4.26±0.05 ^f
[Fe/H]	-0.15±0.04 ^c	0.07±0.04 ^d	0.29±0.16 ^e	0.33±0.11 ^f
R_*/R_\odot	1.065±0.009 ^c	1.483 ^{+0.025} _{-0.029} ^d	1.02±0.03 ^e	1.42±0.07 ^f
M_*/M_\odot	0.913±0.022 ^c	1.166 ^{+0.051} _{-0.054} ^d	1.12±0.07 ^e	1.32±0.09 ^f
K (m/s)	3.3 ^{+0.8} _{-1.0} ^c	48.2 ^{+4.4} _{-4.3} ^d	85±11 ^e	375±13 ^f
M_p from RV (M_J)	0.0145 ^{+0.0040} _{-0.0046}	0.432 ^{+0.053} _{-0.051}	0.560 ^{+0.0986} _{-0.093}	3.23±0.26
Avg 3rd Light (%) ^b	1.13	1.87	4.54	2.97
Transit fit				
T_0 (BJD-2545833)	131.57513±0.00005	171.00915±0.00001	137.18104±0.00002	132.41624±0.00002
b	0.30 ^{+0.21} _{-0.20}	0.168 ^{+0.010} _{-0.012}	0.6846 ^{+0.0046} _{-0.0050}	0.6508 ^{+0.0071} _{-0.0087}
R_p/R_*	0.01247 ^{+0.00031} _{-0.00014}	0.118867 ^{+0.00085} _{-0.00094}	0.10253 ^{+0.00043} _{-0.00045}	0.08628 ^{+0.00036} _{-0.00033}
a/R_*	3.47 ^{+0.13} _{-0.31}	8.019 ^{+0.014} _{-0.013}	5.053±0.021	6.975 ^{+0.047} _{-0.041}
i (Degrees)	85.1 ^{+3.4} _{-4.3}	88.796 ^{+0.088} _{-0.074}	82.214 ^{+0.090} _{-0.085}	84.646 ^{+0.107} _{-0.091}
u_1	0.232 ^{+0.041} _{-0.046}	0.1956 ^{+0.0056} _{-0.0053}	0.210 ^{+0.051} _{-0.050}	0.183 ^{+0.038} _{-0.037}
u_2	-0.005 ^{+0.02} _{-0.03}	0.0293 ^{+0.0043} _{-0.0041}	-0.051 ^{+0.032} _{-0.039}	-0.077 ^{+0.021} _{-0.036}
Phase curve fit				
Best Model	M_p -from-RV	M_p -from-RV + Offset	M_p -from-RV + Offset	M_p -from-Fit + Offset
F_{ecl} (ppm)	7.5 ^{+1.3} _{-1.5}	20.2±4.7	44±12	11 ⁺³² ₋₃₁
A_p (ppm)	9.79 ^{+2.0} _{-1.8}	22.9 ^{+4.3} _{-4.1}	69 ⁺¹⁷ ₋₁₈	71±44
θ (in phase)	...	-0.123±0.016	-0.087±0.014	-0.0747 ^{+0.0074} _{-0.0078}
F_n (ppm)	-2.3 ^{+3.1} _{-3.5}	2.8 ^{+7.8} _{-8.0}	-15 ⁺²⁷ ₋₂₈	-53 ⁺⁷¹ ₋₇₀
M_p (M_J)	6.3 ^{+5.5} _{-5.8}
Derived parameters				
R_p (R_J)	0.1321 ^{+0.0044} _{-0.0026}	1.754 ^{+0.031} _{-0.036}	1.040±0.035	1.219 ^{+0.065} _{-0.064}
a (Au)	0.01720 ^{+0.00081} _{-0.00168}	0.0553 ^{+0.0010} _{-0.0012}	0.02396 ^{+0.00081} _{-0.00080}	0.0460 ^{+0.0026} _{-0.0025}
$A_{\text{g,ecl}}$	0.58 ^{+0.17} _{-0.21}	0.092±0.022	0.108±0.032	0.071 ^{+0.212} _{-0.071}
$T_{\text{eq,max}}$ (K)	2730 ⁺¹⁵⁰ ₋₇₀	1900±30	2260±60	2070±60
$T_{\text{eq,hom}}$ (K)	2130 ⁺¹²⁰ ₋₆₀	1480±30	1770±50	1620±40
$T_{\text{B,day}}$ (K)	3300±100	2150 ⁺⁷⁰ ₋₈₀	2400±100	2200 ⁺⁴⁰⁰ ₋₂₂₀₀
$T_{\text{B,night}}$ (K)	<2400(1 σ) <3000(2 σ)	<2000(1 σ) <2100(2 σ)	<2100(1 σ) <2400(2 σ)	<2300(1 σ) <2800(2 σ)

^a From the NASA Exoplanet Archive (Akeson et al. 2013).

^b From the Kepler Input Catalog.

^c From Batalha et al. (2011).

^d From Fortney et al. (2011).

^e From Santerne et al. (2011).

^f From Bonomo et al. (2012).

4.5. Kepler-91b/KOI-2133.01

For Kepler-91b our transit parameters differed significantly from our results in E13. Previously we found a low impact parameter, consistent with zero, an a/R_* of 4.51, an inclination of 89.9° and a R_p/R_* of 0.01775. These values, in combination with a measured eclipse depth of 38.7 ppm, resulted in a geometric albedo >1 and therefore led us to conclude that Kepler-91b, previously referred to as KOI-2133, was a self-luminous object, not a planet. In this study we find an impact parameter of 0.9442, an a/R_* of 1.873 and a R_p/R_* of 0.02036. These, along with our new eclipse depth of 47 ppm, results in a geometric albedo of 0.39, which is fully consistent with Kepler-91b being a planet.

Independent studies of Kepler-91b also find differing transit parameters. Lillo-Box et al. (2013) find a high b set of solutions, similar to this study, while Sliski & Kipping (2014) find a low b set of solutions, similar to E13.

The transit shapes of both sets of solutions are very similar. With a depth of approximately 400 ppm and

only long-cadence observations, the transit light curve of Kepler-91b appears to be only marginally constrained enough to measure the subtle differences between these models. We found that, by using varying subsets of the Kepler-91b light curve, we could obtain solution sets with both the low and high impact parameters. However, using the full 18 quarters of available data, the high impact parameter set of solutions were strongly favoured. Therefore the variations between different studies could be due to residual systematics and/or stellar variability. Other differences between studies include the orbital period as well as the removal method of systematics and outliers: Sliski & Kipping (2014) derive an orbital period of 6.246733±0.000005 days, while our studies and Lillo-Box et al. (2013) assume a value of 6.24658±0.00008 days.

In E13 we find an eclipse depth of 38.7±8.2, in agreement with our current value, while Lillo-Box et al. (2013) attribute the dip near $\phi=0.5$ to stellar variability and therefore do not include a secondary eclipse in their fit. However, they do predict a theoretical secondary

TABLE 6
STELLAR AND PLANETARY PARAMETERS

Parameter	Kepler-76b	Kepler-91b	Kepler-412b	TrES-2b
KOI	1658.01	2133.01	202.01	1.01
Period (days) ^a	1.5449298±0.0000004	6.24658±0.00008	1.7208604±0.0000003	2.47061317±0.00000009
T_* (K)	6409±95 ^c	4605±97 ^d	5750±90 ^e	5850±50 ^f
log g (cgs)	4.2±0.3 ^c	2.936±0.013 ^d	4.30±0.07 ^e	4.426 ^{+0.021} _{-0.023} ^f
[Fe/H]	-0.1±0.2 ^c	0.290±0.162 ^d	0.27±0.12 ^e	-0.15±0.10 ^f
R_*/R_\odot	1.32±0.08 ^c	6.528±0.352 ^d	1.287±0.035 ^e	1.000 ^{+0.036} _{-0.033} ^f
M_*/M_\odot	1.2±0.2 ^c	1.34±0.17 ^d	1.167±0.091 ^e	0.980±0.062 ^f
K (m/s)	306±20 ^c	...	142±11 ^e	181.3±2.6 ^g
M_p from RV (M_J)	2.01 ^{+0.37} _{-0.35}	...	0.941 ^{+0.125} _{-0.019}	1.197±0.068
Avg 3rd Light (%) ^b	5.55	1.00	5.96	0.729
Transit fit				
T_0 (BJD-2545833)	133.54841 ^{+0.00001} _{-0.00002}	136.3958±0.0002	133.02122±0.00002	122.763360 ^{+0.000003} _{-0.000002}
b	0.96226 ^{+0.0040} _{-0.0049}	0.9442 ^{+0.0024} _{-0.0029}	0.7942 ^{+0.0028} _{-0.0032}	0.84359 ^{+0.00075} _{-0.00062}
R_p/R_*	0.1033 ^{+0.0024} _{-0.0030}	0.02036 ^{+0.00033} _{-0.00023}	0.10474 ^{+0.00054} _{-0.00077}	0.12539 ^{+0.00049} _{-0.00035}
a/R_*	4.464 ^{+0.049} _{-0.041}	1.873 ^{+0.029} _{-0.026}	4.841 ^{+0.024} _{-0.023}	7.903 ^{+0.019} _{-0.016}
i (Degrees)	77.55 ^{+0.20} _{-0.17}	59.73 ^{+0.61} _{-0.55}	80.559 ^{+0.084} _{-0.079}	83.872 ^{+0.020} _{-0.018}
u_1	0.236 ^{+0.042} _{-0.052}	0.179 ^{+0.041} _{-0.028}	0.204±0.081	0.189 ^{+0.042} _{-0.040}
u_2	0.291 ^{+0.030} _{-0.049}	0.208 ^{+0.030} _{-0.022}	-0.043 ^{+0.061} _{-0.043}	-0.048 ^{+0.022} _{-0.030}
Phase curve fit				
Best Model	M_p -from-RV + Offset	M_p -from-Fit	M_p -from-RV	M_p -from-RV
F_{ecl} (ppm)	131.6 ^{+6.1} _{-6.3}	47±18	53±14	7.7±1.8
A_p (ppm)	106.9 ^{+4.3} _{-4.4}	48 ⁺¹⁸ ₋₁₉	31±14	4.1 ^{+1.1} _{-1.0}
θ (in phase)	0.0230±0.0034
F_n (ppm)	28 ⁺¹⁰ ₋₁₁	-2±40	22±28	3.6±2.8
M_p (M_J)	...	0.455±0.086
Derived parameters				
R_p (R_J)	1.36±0.12	1.322 ^{+0.094} _{-0.086}	1.341 ^{+0.044} _{-0.046}	1.247 ^{+0.050} _{-0.045}
a (Au)	0.0274 ^{+0.0020} _{-0.0019}	0.0569 ^{+0.0040} _{-0.0038}	0.02897 ^{+0.00093} _{-0.00092}	0.0367 ^{+0.0014} _{-0.0013}
$A_{g,\text{ecl}}$	0.246 ^{+0.033} _{-0.026}	0.39 ^{+0.18} _{-0.17}	0.113 ^{+0.034} _{-0.031}	0.0307 ^{+0.0074} _{-0.0073}
$T_{\text{eq,max}}$ (K)	2740 ⁺⁵⁰ ₋₆₀	3040±90	2360±40	1880±20
$T_{\text{eq,hom}}$ (K)	2140±40	2380±70	1850±30	1470±10
$T_{\text{B,day}}$ (K)	2890 ⁺⁷⁰ ₋₆₀	3200 ⁺²⁰⁰ ₋₃₀₀	2400±100	1910 ⁺⁵⁰ ₋₆₀
$T_{\text{B,night}}$ (K)	2380 ⁺¹³⁰ ₋₁₅₀	<3100(1 σ) <3500(2 σ)	<2400(1 σ) <2600(2 σ)	1770 ⁺¹¹⁰ ₋₂₂₉

^a From the NASA Exoplanet Archive (Akeson et al. 2013).

^b From the Kepler Input Catalog.

^c From Faigler et al. (2013).

^d From Huber et al. (2013).

^e From Deleuil et al. (2014).

^f From Sozzetti et al. (2007).

^g From O'Donovan et al. (2006).

eclipse depth of 25 ± 15 ppm, which is in agreement with our current value. There are also several other large dips in the phase curve, the largest of which are centred around a phase of 0.17 and 0.7. We therefore caution the use of the parameters derived from our eclipse value (see Section 4.8). Lillo-Box et al. (2013) also find an eccentricity of $0.066^{+0.013}_{-0.017}$, while our fit did not favour an eccentric model.

4.6. Comparison to Previous Studies

As the number of published phase curve measurements rapidly increases, it is becoming nearly impossible to coherently compare individual results. Instead we choose to compare all published phase curve measurements, for each of the four components, at once.

In Table 1 we present all $>1\sigma$ published *Kepler* eclipse depths, phase function, ellipsoidal (A_e) and Doppler boosting (A_d) amplitudes for the 14 planets in our sample. In this table we have presented all phase function measurements as peak-to-peak amplitudes and all ellip-

soidal and Doppler measurements as semi-amplitudes. In addition we have adjusted the amplitudes for KOI-13b from E13, A14 and Shporer et al. (2011), to account for a dilution factor of 1.913 ± 0.019 (see Section 2.2).

For all measurements, where errors were reported, we calculate a σ deviation between the published values and our results. Note that our A_e and A_d values are derived from planet mass measurements and are therefore not independent. A histogram of the differences can be found in Fig. 6.

For three components (A_{ecl} , A_p , A_e) the majority of the published values lie within 1σ , while for A_d most previous values lie within 2σ and are skewed toward higher values. There are also some notable outliers. For the eclipse depth, early measurements of HAT-P-7b from Borucki et al. (2009) and for KOI-13b from Coughlin & López-Morales (2012) and Szabó et al. (2011) differ by more than 5σ . However, it should be noted that these studies all used significantly less data than ours. The phase function of KOI-13b from E13 is 3σ lower than our value, while the phase function of

TABLE 7
STELLAR AND PLANETARY PARAMETERS

Parameter	HAT-P-7b		KOI-13b	
		Model 1	Model 2	Model 3
KOI	2.01		13.01	
Period (days) ^a	2.2047354±0.0000001		1.763588±0.000001	
T_* (K)	6350±80 ^c	7650±250 ^d	9107 ⁺²⁵⁷ ₋₄₂₅ ^e	8511±1 ^f
log g (cgs)	4.07 ^{+0.04} _{-0.08} ^c	4.2±0.5 ^d	3.867 ^{+0.235} _{-0.148} ^e	3.9±0.1 ^f
[Fe/H]	0.26±0.08 ^c	0.2±0.2 ^d	0.070 ^{+0.140} _{-0.650} ^e	0.2±0.1 ^f
R_*/R_\odot	1.84 ^{+0.23} _{-0.11} ^c	1.74±0.04 ^d	3.031 ^{+1.198} _{-0.944} ^e	2.55±0.1 ^f
M_*/M_\odot	1.47 ^{+0.08} _{-0.05} ^c	1.72±0.10 ^d	2.47 ^{+0.45} _{-0.72} ^e	2.05±0.1 ^f
K (m/s)	213.5±1.9 ^c
M_p from RV (M_J)	1.781 ^{+0.081} _{-0.056}
Avg 3rd Light (%) ^b	0.184	...	0.142	...
Transit fit				
T_0 (BJD-2545833)	121.358572±0.000004		120.56596 ^{+0.00002} _{-0.00003}	
b	0.4960 ^{+0.0011} _{-0.0013}	0.2536 ^{+0.0038} _{-0.0035}	0.2537 ^{+0.0037} _{-0.0034}	0.2535 ^{+0.0033} _{-0.0034}
R_p/R_*	0.077524 ^{+0.000017} _{-0.000022}	0.087373 ^{+0.000023} _{-0.000024}	0.087373 ^{+0.000025} _{-0.000025}	0.087371 ^{+0.000022} _{-0.000023}
a/R_*	4.1545 ^{+0.0029} _{-0.0025}	4.5007 ^{+0.0039} _{-0.0040}	4.5008 ^{+0.0039} _{-0.0042}	4.4987 ^{+0.0046} _{-0.0054}
i (Degrees)	83.143 ^{+0.023} _{-0.020}	86.770 ^{+0.048} _{-0.052}	86.769 ^{+0.046} _{-0.050}	86.770 ^{+0.047} _{-0.046}
u_1	0.1747 ^{+0.0022} _{-0.0021}	0.1678±0.0015	0.1678 ^{+0.0016} _{-0.0017}	0.1678±0.0015
u_2	0.0003±0.002	-0.0173±0.0013	-0.0173±0.0014	-0.0173±0.0013
Phase curve fit				
Best Model	Mp-from-Fit + Offset + 3rd Harmonic	Eccentric + Mp-from-Fit + 3rd Harmonic ... + Offset		
F_{ecl} (ppm)	71.2±1.5	172.0±1.8	170.8±1.5	170.8±7.6
A_p (ppm)	73.3±2.7	151.9 ^{+1.1} _{-1.0}	150.4±2.7	150±11
θ (in phase)	0.01935 ^{+0.00080} _{-0.00082}	...	0.00178±0.00052	0.00280±0.00053
F_b (ppm)	-1.1 ^{+4.1} _{-4.2}	20.2±2.8	20.6 ^{+4.1} _{-4.2}	21±19
M_p (M_J)	1.625 ^{+0.082} _{-0.079}	9.3±0.0	12.826 ^{+0.082} _{-0.079}	9.96±0.0
A_3 (ppm)	-1.93±0.23	-7.03±0.27	-7.14±0.26	-7.33±0.27
θ_3 (in phase)	0.0163 ^{+0.0054} _{-0.0052}	-0.0840±0.0024	-0.0908 ^{+0.1649} _{-0.0038}	-0.09880 ^{+0.0025} _{-0.0026}
e	...	0.00064 ^{+0.00012} _{-0.00016}	0.00064 ^{+0.00012} _{-0.000098}	0.00074 ^{+0.00110} _{-0.00016}
ω (Degrees)	...	9±20	-1 ⁺³⁰ ₋₁₀	18 ⁺⁵³ ₋₁₃
Derived parameters				
R_p (R_J)	1.419 ^{+0.178} _{-0.085}	1.512±0.035	2.63 ^{+1.04} _{-0.82}	2.216±0.087
a (Au)	0.0355 ^{+0.0045} _{-0.0021}	0.03641±0.00087	0.063 ^{+0.025} _{-0.020}	0.0533 ^{+0.0021} _{-0.0022}
$A_{g,\text{ecl}}$	0.2044 ^{+0.0046} _{-0.0048}	0.4565 ^{+0.0057} _{-0.0058}	0.4532 ^{+0.0050} _{-0.0052}	0.453±0.021
$T_{\text{eq,max}}$ (K)	2820±40	3300±100	3900 ⁺¹⁰⁰ ₋₂₀₀	3626 ⁺³ ₋₂
$T_{\text{eq,hom}}$ (K)	2200±30	2550±80	3040 ⁺⁹⁰ ₋₁₄₀	2837±2
$T_{\text{B,day}}$ (K)	2860±30	3490 ⁺⁶⁰ ₋₇₀	3830 ⁺⁵⁰ ₋₉₀	3710±30
$T_{\text{B,night}}$ (K)	<2000(1 σ) <2200(2 σ)	2587 ⁺⁷⁷ ₋₈₄	2790 ⁺⁹⁸ ₋₁₃₀	2730 ⁺²⁵⁰ ₋₆₁₀

Note: For KOI-13b values were reported for three sets of stellar parameters from the literature, where our chosen values from Shporer et al. (2014). A stellar mass uncertainty of $\pm 0.1M_\odot$ and a stellar radius uncertainty of $\pm 0.1R_\odot$ was assumed when not given in the literature.

^a From the NASA Exoplanet Archive (Akeson et al. 2013).

^b From the Kepler Input Catalog.

^c From Pál et al. (2008).

^d From Shporer et al. (2014).

^e From Huber et al. (2013).

^f From Szabó et al. (2011).

HAT-P-7b from A14 is 5σ lower. The Doppler boosting measurements for HAT-P-7b also vary significantly from E13 and A14, which find values 14 and 15σ higher than our results. The same is true for Kepler-76b, where the Doppler boosting signal from A14 and Faigler et al. (2013) is 7 and 5σ higher. The eclipse depth for Kepler-76b also differs significantly from previous studies but this is most likely because our model fits for the planet's surface brightness, which accounts the partial eclipse of Kepler-76b (see Section 4.4).

It is unclear why our phase function result for KOI-13b is higher than previously, but it is in agreement with values from A14 and Shporer et al. (2011). For Doppler

boosting it is possible that the inclusion of a peak phase function offset is the source of this discrepancy. To investigate if there is a degeneracy between these two parameters we refit each planet with the ellipsoidal and Doppler amplitude as independent parameters. We find that there is a correlation between the measured Doppler amplitude and phase function offset, for small offsets, where an underestimated Doppler signal corresponds to a positive offset (i.e. a peak before the eclipse).

For HAT-P-7b and Kepler-76b we find a positive offset of 0.019 and 0.023, respectively. Since these offsets were not included in previous studies it could explain why we find significantly lower Doppler amplitudes for these

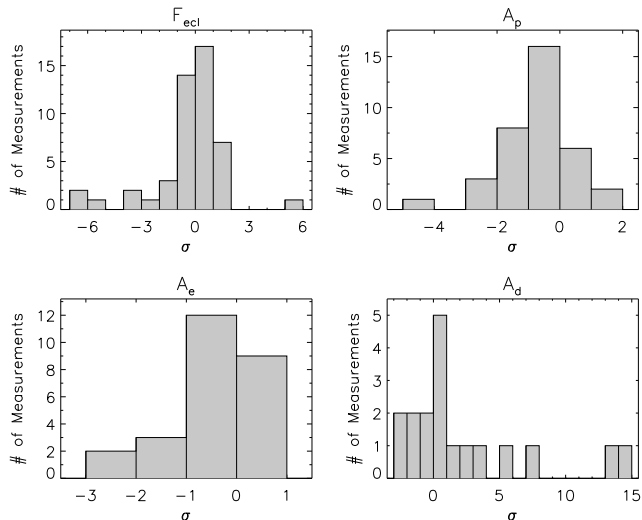


FIG. 6.— Histogram of the σ deviation between published values with reported errors and our results (see Table 1) for eclipse depths (F_{ecl}), phase function amplitudes (A_p), ellipsoidal variations (A_e) and Doppler boosting (A_d).

two planets. Note that A14 also fit for a peak offset but do not find any positive offsets. This is somewhat expected as they fit for ellipsoidal variations and Doppler boosting independently and therefore a small positive offset would be modeled as an increase in Doppler signal.

4.7. 3rd Harmonic and Spin-Orbit Misalignment

Since a third order harmonic is clearly visible for KOI-13b, we refit each planet using phase curve model that includes a third cosine harmonic as described in Section 3. For three of our targets (Kepler-7b, HAT-P-7b and KOI-13b) we found that the BIC favoured a model with this additional component. However, after refitting to different sub-samples of Kepler-7b’s data we conclude that the signal is not coherent in time and therefore exclude this component.

For KOI-13b we measure a third harmonic in agreement with our previous value from E13 and out of phase by 2σ . However, the errors for the amplitude and phase of the third harmonic (see Table 7) were obtained from our MCMC simulations and our bootstrap analysis has shown these to be consistently underestimated. Shporer et al. (2014) chose to model this feature by including a second and third sine harmonic as well as a third cosine harmonic. Combined their model produces a third harmonic ~ 3 ppm less than ours with a relative phase shift of ~ 0.1 .

The cause of this additional third harmonic could be the movement of the stellar tidal bulge raised by the planet, the source of ellipsoidal variations, across areas of the star with different surface brightnesses. The motivation for this reasoning is the asymmetry in KOI-13b’s transit caused by a spin-orbit misalignment (Szabó et al. 2011; Barnes et al. 2011) and significant gravity darkening due to rapid stellar rotation ($v \sin i = 65\text{--}70 \text{ km s}^{-1}$; Szabó et al. 2011).

For HAT-P-7b we find that the BIC favours a model including a 8σ detection of a 1.93 ppm third harmonic.

Interestingly, similar to E13, Van Eylen et al. (2013) and Morris et al. (2013), we find an asymmetry in HAT-P-7b’s transit. Analysis of this asymmetry is outside the scope of this paper, but, like KOI-13b, it could be related to the system’s significant spin-orbit misalignment (Winn et al. 2009; Narita et al. 2009). Although, unlike KOI-13b’s host star, HAT-P-7 has an unusually low, and somewhat disputed, $v \sin i$ of $2\text{--}6 \text{ km s}^{-1}$, indicating a nearly pole-on view (Winn et al. 2009; Narita et al. 2009; Albrecht et al. 2012; Torres et al. 2012).

4.8. Planet Brightness, Temperature and Albedo

Using our eclipse depths we calculate each planet’s geometric albedo assuming only reflected light (A_g) and the brightness temperature of the day and night side ($T_{\text{B,day}}$ and $T_{\text{B,night}}$) assuming only thermal emission. We also calculate the equilibrium temperature, assuming only no reflected light, for the two limiting cases, instant re-radiation ($f=2/3$, $T_{\text{eq,max}}$) and homogeneous re-distribution ($f=1/4$, $T_{\text{eq,hom}}$). These values can be found in Tables 4-7, their detailed description in E13 and references therein.

For Kepler-10b, Kepler-91b and KOI-13b we find geometric albedos of 0.58, 0.39 and 0.46, respectively, while for all the other planets we find albedos less than 0.25. Kepler-10b’s very high albedo is a clear outlier from our sample, as is its small radius, at only $1.4R_{\oplus}$, ultra short period and rocky composition (Batalha et al. 2011).

For Kepler-91b these findings differ largely from E13, where we found an unphysical albedo due to our significantly different a/R_{\star} values. However, note that the validity of Kepler-91b’s measured eclipse depth and derived albedo is uncertain as the phase curve exhibits large variations due to stellar variability and/or residual systematics (see Section 4.5).

For KOI-13b the high albedo could instead be a result of thermal emission as KOI-13b’s blackbody peaks in the *Kepler* bandpass. However, the thermal contribution depends heavily on which of the three sets of stellar parameters are assumed (see Section 4.3). This is discussed in more depth later in this section. Since the eclipse depths at optical wavelengths are likely a combination of reflected light and thermal emission, we self-consistently solve for A_g taking into account both contributions using

$$F_{\text{ecl}} = \left(\frac{R_p}{R_{\star}}\right)^2 \frac{\int B_{\lambda}\{T_{\star}\left(\frac{a}{R_{\star}}\right)^{-1/2}[f(1-\frac{3}{2}A_g)]^{1/4}\} T_{\text{K}} d\lambda}{\int (T_{\text{K}} F_{\lambda,\star}) d\lambda} + A_g \left(\frac{R_p}{a}\right)^2 \quad (18)$$

where B_{λ} is the Planck function of the equilibrium temperature expression in parentheses, T_{K} is the Kepler transmission function and $F_{\lambda,\star}$ is the stellar flux computed using the NEXTGEN model spectra (Hauschildt et al. 1999). Here we have assumed that the Bond albedo is $\frac{3}{2}A_g$.

f We calculate each target’s self-consistent albedo and corresponding temperature for the two limiting cases, denoted *max* and *hom*, and present the values in Table 8. For several planets we find that the self-consistent albedo, in the instant re-radiation limit, is marginally consistent with zero, meaning that thermal

TABLE 8
SELF-CONSISTENT ALBEDOS AND TEMPERATURES

	Self-Consistent				Reflected Light Fraction	
	$A_{g,max}$	T_{max}	$A_{g,hom}$	T_{hom}	$f_{ref,max}$	$f_{ref,hom}$
Kepler-5b	$0.067^{+0.039}_{-0.042}$	2182^{+63}_{-60}	$0.118^{+0.026}_{-0.025}$	1670^{+38}_{-39}	$0.549^{+0.451}_{-0.042}$	$0.9706^{+0.029}_{-0.025}$
Kepler-6b	$0.049^{+0.031}_{-0.032}$	1827 ± 40	0.069 ± 0.026	1419^{+28}_{-29}	$0.706^{+0.294}_{-0.032}$	$0.9849^{+0.015}_{-0.026}$
Kepler-7b	$0.232^{+0.062}_{-0.067}$	1870 ± 86	$0.247^{+0.055}_{-0.058}$	1450^{+61}_{-63}	0.933 ± 0.067	$0.99643^{+0.0036}_{-0.0575}$
Kepler-8b	$0.094^{+0.058}_{-0.072}$	2060^{+120}_{-110}	0.131 ± 0.042	1589^{+71}_{-72}	$0.708^{+0.292}_{-0.072}$	$0.9820^{+0.018}_{-0.042}$
Kepler-10b	$0.583^{+0.083}_{-0.277}$	1620^{+850}_{-1620}	$0.584^{+0.082}_{-0.217}$	1270^{+580}_{-1270}	$0.99794^{+0.0021}_{-0.2765}$	$1.00^{+0.00}_{-0.22}$
Kepler-12b	$0.071^{+0.029}_{-0.032}$	1845^{+57}_{-55}	0.091 ± 0.022	1432 ± 39	$0.775^{+0.225}_{-0.032}$	$0.9882^{+0.012}_{-0.022}$
Kepler-41b	$0.044^{+0.060}_{-0.044}$	2220^{+99}_{-110}	$0.104^{+0.034}_{-0.035}$	1695^{+72}_{-71}	$0.407^{+0.593}_{-0.044}$	$0.9611^{+0.039}_{-0.035}$
Kepler-43b	$0.030^{+0.244}_{-0.030}$	2043^{+79}_{-282}	$0.069^{+0.214}_{-0.069}$	1574^{+86}_{-203}	$0.423^{+0.577}_{-0.030}$	$0.9649^{+0.035}_{-0.069}$
Kepler-76b	$0.144^{+0.074}_{-0.0967}$	2580^{+160}_{-150}	$0.239^{+0.036}_{-0.030}$	1920^{+71}_{-79}	$0.58^{+0.41}_{-0.097}$	$0.9711^{+0.029}_{-0.030}$
Kepler-91b	$0.31^{+0.27}_{-0.31}$	2610^{+520}_{-819}	0.39 ± 0.19	1910^{+330}_{-520}	$0.78^{+0.22}_{-0.31}$	$0.9864^{+0.014}_{-0.188}$
Kepler-412b	$0.031^{+0.064}_{-0.031}$	2334^{+70}_{-102}	$0.107^{+0.036}_{-0.034}$	1769^{+58}_{-60}	$0.271^{+0.729}_{-0.031}$	$0.9506^{+0.049}_{-0.034}$
TrES-2b	$0.0049^{+0.0116}_{-0.0049}$	1877^{+21}_{-27}	0.0293 ± 0.0076	1455^{+18}_{-19}	$0.1591^{+0.5478}_{-0.0049}$	$0.95480^{+0.0452}_{-0.0076}$
HAT-P-7b	$0.047^{+0.045}_{-0.047}$	2764^{+87}_{-86}	$0.1937^{+0.0067}_{-0.0073}$	2022^{+34}_{-33}	$0.228^{+0.229}_{-0.047}$	$0.9478^{+0.0522}_{-0.0073}$
KOI-13b ^a	$0.404^{+0.030}_{-0.079}$	2580^{+270}_{-160}	$0.4529^{+0.0072}_{-0.0083}$	1919^{+83}_{-79}	0.884 ± 0.079	$0.99206^{+0.0079}_{-0.0083}$
KOI-13b ^b	$0.00^{+0.37}_{-0.00}$	3880^{+110}_{-850}	$0.441^{+0.010}_{-0.013}$	2310^{+100}_{-130}	$0.00^{+0.82}_{-0.00}$	$0.9736^{+0.026}_{-0.013}$
KOI-13b ^c	$0.316^{+0.061}_{-0.078}$	3090^{+160}_{-150}	0.445 ± 0.023	2154^{+56}_{-60}	$0.698^{+0.177}_{-0.078}$	$0.9833^{+0.017}_{-0.023}$

Derived using stellar parameters from:

- ^a Shporer et al. (2014).
- ^b Huber et al. (2013).
- ^c Szabó et al. (2011).

emission alone can explain their observed eclipse depths. This can be seen in upper left panel of Fig. 7 where we compare the maximum equilibrium temperature to the reflection only geometric albedo ($A_{g,max}$) and in the upper right panel of Fig. 7 where we compare the equilibrium temperature to the self-consistent geometric albedo. For several planets taking into account the thermal emission significantly lowers the albedo, with many consistent with zero, meaning that their non-zero albedos can be explained with thermal emission.

For KOI-13b we calculate the albedos and temperatures using three sets of stellar parameters reported in the literature (see Section 4.3). These three studies report a stellar temperature between 7650K and 9100K corresponding to an equilibrium temperature from 3300K to 3900K. This leads to a large variation in the self-consistent albedo, ranging from 0 to 0.4.

We also compare the day-side brightness temperature ($T_{B,day}$) to the maximum equilibrium temperature (see lower left panel of Fig. 7) and find that for several planets the brightness temperature is significantly higher than the equilibrium temperature. This excess brightness temperature can be accounted for if we include a reflected light contribution as, at optical wavelengths, even low albedos can produce a reflected light dominated brightness. This is supported by our finding that for all planets the self-consistent albedo is < 1 .

There doesn't appear to be a correlation between the excess brightness temperature and equilibrium temperature as an excess is seen in both the hottest and coolest planets in our sample. It is possible is that this extra flux is seen because we are probing significantly hotter layers of the planet's atmosphere, which is supported by our finding that for Kepler-76b, TrES-2b and KOI-13b we need an increase in brightness to explain both their observed day- and night-side flux (see Section 4.9).

4.9. Night-side Emission

Since the eclipse depth provides a day-side brightness and the phase function amplitude measures the day-night flux difference we can place some constraint on the planet's night-side brightness. Note that for the planets with a phase function offset we calculate the difference between the eclipse depth and phase function amplitude at $\phi=0.5$, not the peak amplitude. For almost all of our planets the night-side flux was marginally consistent with zero with the exception of Kepler-76b, TrES-2b and KOI-13b, which have 3, 1 and 7σ detections, respectively. Note that for Kepler-76b the eclipse does not appear much larger than the phase function (see Figure 5). However, compensating for its partial eclipse leads to a larger derived eclipse depth and therefore a significant night-side flux (see Section 4.4)

By combining the day and night side measurements it is possible to place a constraint on the planet's redistribution factor (f') by simultaneously solving for f' and $A_{g,max}$ in the following equations

$$F_{ecl} = \left(\frac{R_p}{R_*}\right)^2 \frac{\int B_\lambda \left\{ T_* \left(\frac{a}{R_*}\right)^{-1/2} \left[\left(\frac{1}{4} + f'\right) \left(1 - \frac{3}{2} A_g\right)\right]^{1/4} \right\} T_K d\lambda}{f(T_K F_{\lambda,*} d\lambda)} + A_g \left(\frac{R_p}{a}\right)^2 \quad (19)$$

$$F_n = \left(\frac{R_p}{R_*}\right)^2 \frac{\int B_\lambda \left\{ T_* \left(\frac{a}{R_*}\right)^{-1/2} \left[\left(\frac{1}{4} - f'\right) \left(1 - \frac{3}{2} A_g\right)\right]^{1/4} \right\} T_K d\lambda}{f(T_K F_{\lambda,*} d\lambda)} \quad (20)$$

where $f'=1/4$ corresponds maximum day-side and zero night-side temperature, while $f'=0$ is an equal day-night temperature. For planets with a marginal night-side detection, Kepler-8b, Kepler-12b and Kepler-412b, we find albedos of $0.13^{+0.06}_{-0.08}$, $0.09^{+0.03}_{-0.04}$ and $0.11^{+0.05}_{-0.08}$, respectively, but do not find any constraint on f' .

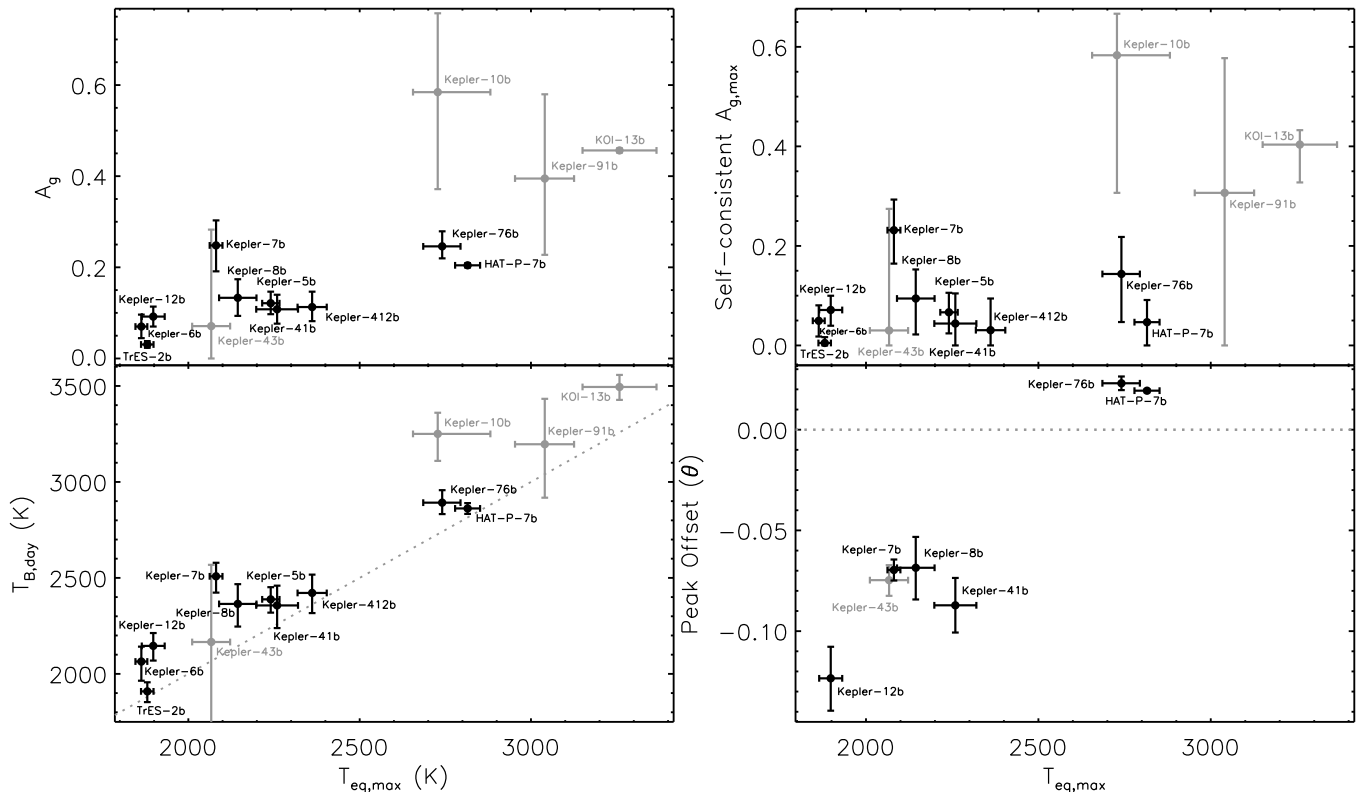


FIG. 7.— Secondary eclipse derived planet properties plotted as a function of the maximum equilibrium temperature: Top left, geometric albedo (assuming only reflected light); Top right, self-consistent geometric albedo (accounting for both reflected light and thermal emission); Bottom left, day-side brightness temperature (assuming only thermal emission), where the dotted grey line indicates equal brightness and equilibrium temperatures; Bottom right, peak offset of the planet’s phase function, where the dotted grey line indicates the boundary between eastward and westward shifts. The grey points indicate values that are in doubt due to light curve variability (Kepler-43b and Kepler-91b), differ in composition compared to the rest of our sample (Kepler-10b) or are strongly influenced by the chosen stellar parameters (KOI-13b).

For the planets with a significant night-side flux (Kepler-76b, TrES-2b and KOI-13b) our simple model fails, and we do not find any solution. This is most likely due to the assumption that the atmosphere is isothermal, with two temperatures, one for the day-side and one for the night-side. However, this can be accounted for if we are probing a significantly hotter layer of the planet’s atmosphere in the *Kepler* bandpass.

4.10. Peak Offset of Planetary Light

For seven of our fourteen targets the BIC favoured the inclusion of an offset of the phase function peak from mid-eclipse. Of this sample, the five cooler planets (Kepler-7b, -8b, -12b, -41b and -43b) have phase functions peaked after eclipse, referred to as a negative offset in our formalism, while the two hotter planets (Kepler-76b and HAT-P-7b) reach peak brightness before eclipse (positive offset).

Physically, a peak after eclipse corresponds to a westward shift of the planet’s peak surface brightness from the substellar point, which, for tidally locked planets, would mean that the planet appears brightest on the morning-side, when some of the night-side is still in view, instead of at noon when the full day-side is visible. A peak before eclipse would be the opposite, an eastward shift or a maximum brightness in the evening.

Of these planets only three (Kepler-7b, -12b and -43b) have published offset measurements. For Kepler-7b, Demory et al. (2013) find an offset of -0.114 ± 0.033 , while A14 find an offset of -0.08 . These measurements differ by 2σ from our value of -0.070 ± 0.005 . However, each study uses a slightly different number of quarters, between 14 and 18, utilizes different methods for the removal of systematics and varies on how they model Doppler boosting and ellipsoidal variations. Nonetheless it is clear that each study finds a significant westward shift.

A14 find a peak offset for Kepler-12b and Kepler-43b of -0.19 and -0.10 , respectively, significantly higher than our values of -0.12 ± 0.02 and 0.075 ± 0.007 . They also do not find an offset for the other four planets in our sample, possibly due to the degeneracy between the Doppler boosting amplitude and phase function offset (see Section 4.2).

When we compare our measured peak offsets to the planet’s equilibrium temperature (see lower right panel of Fig. 7) we see a division between planets around an equilibrium temperature of approximately 2500K, where hotter planets have a positive or eastward shift and cooler planets have a negative or westward shift.

For tidally locked hot-Jupiters, with a thermal emission dominated brightness, a robust outcome of a variety of circulation models (e.g. Cooper & Showman

2005; Heng et al. 2011) combined with analytical theory (Showman & Polvani 2011) is an eastward shift of the planet’s peak brightness. Demory et al. (2013) use this, the lack of significant thermal emission in the *Spitzer* 3.6 and 4.5 μm bandpasses and the presence of a westward shift to conclude that Kepler-7b’s phase curve is dominated by reflected light. Furthermore they state that the most likely cause of the westward shift is the presence of inhomogeneous reflective clouds, whose properties change as a function of longitude and are influenced by the planet’s wind and thermal patterns.

4.11. Determining a Reflected Light Fraction with *Kepler*

The self-consistent albedo measurements give strong evidence that, for most planets, the light from the planet in the *Kepler* band is a combination of both reflected light and thermal emission. Since *Kepler* observes in a single broad optical band, it is difficult to constrain the relative contributions from each source. However, using our self-consistent albedo equation we can estimate the reflected light fraction (f_{ref}) by dividing the observed geometric albedo by our self-consistent albedo. The values for the two limiting cases can be found in Table 8.

In the left panel of Fig. 8 we compare the reflected light fraction and maximum equilibrium temperature and do not find a significant correlation. This is not surprising as most, if not all, values are not well constrained and several are completely unconstrained.

For the seven planets with peak offsets of their planetary light, we compare the reflected light fraction and peak offset in the right panel of Fig. 8. For the three planets with a westward offset and a constraint on their reflected light fraction (Kepler-7b, -8b and 12b), it appears that at least some reflectivity is needed explain their observed brightnesses.

For HAT-P-7b we measure an eastward offset and find that its brightness can be marginally explained by thermal emission alone while for Kepler-76b, which also exhibits an eastward offset, at least some reflected light is required. We note that for Kepler-76b we derived an eclipse depth larger than exhibited in the phase curve, due to compensating for Kepler-76b’s partial eclipse (see Section 4.4). However, if we do not compensate for this, the eclipse depth can be explained solely by thermal emission. Therefore it is important to properly treat the partial eclipse when determining the reflectivity of Kepler-76b.

4.12. Inhomogeneous Clouds vs. Shifted Hot-Spot

With *Kepler* alone we are not able to determine whether planets with a peak offset are dominated by reflected light or thermal emission. However, if an equilibrium temperature of approximately 2500K is an upper boundary on cloud formation (e.g. Fortney et al. 2008ab; Morley et al. 2013), the phase functions of Kepler-76b and HAT-P-7b would be dominated by thermal emission and therefore our measurement of an eastward shift is consistent with theory (see Section 4.10). On the other hand, if the planets under 2500K are able to condense particles, it is possible that their phase functions and

westward shifts are caused by inhomogeneous reflective clouds as seen in Kepler-7b (Demory et al. 2013).

For tidally locked planets, a westward offset (or a peak after eclipse) means that the planet appears brightest on the morning-side. If this morning-side brightness is produced by reflective clouds, it is conceivable that these clouds could condense on the night-side, when temperatures are cooler, and then dissipate as the atmosphere heats up during the day, thus resulting in thicker, more reflective clouds at sunrise that gradually disperse throughout the day.

5. CONCLUSIONS

From our analysis of phase variations in fourteen *Kepler* planets, with significant detections in each of the phase curve components, we find that most have low geometric albedos <0.25 dominated by reflected light, with the exception of Kepler-10b, Kepler-91b and KOI-13b where we derive values of 0.58, 0.39 and 0.46, respectively. Of our targets, KOI-13b, with a small eccentricity of $6.4^{+1.2}_{-1.6} \times 10^{-4}$, is the only planet where an eccentric orbit is favoured.

For KOI-13b, we again detect a third cosine harmonic with an amplitude of 7.0 ± 0.3 ppm and for HAT-P-7b we detect a never-before-seen third harmonic with an amplitude of 1.9 ± 0.2 ppm. The cause of this additional third harmonic could be the movement of the stellar tidal bulge raised by the planet, the source of ellipsoidal variations, across areas of the star with different surface brightnesses. The motivation for this reasoning is the asymmetry in KOI-13b’s and HAT-P-7b’s transit, where the former is caused by a spin-orbit misalignment and significant gravity darkening due to rapid stellar rotation.

Our re-analysis of Kepler-91b’s transit found very different results than in E13, where we previously derived a geometric albedo >1 and therefore concluded that Kepler-91b, previously referred to as KOI-2133, was a self-luminous object, not a planet. However, with our new set of transit parameters, along with our new eclipse depth of 47 ppm, we derive a geometric albedo of 0.39, fully consistent with it being a planet.

Our bootstrap analysis revealed that MCMC fits consistently underestimate uncertainties caused by light curve variations either from residual instrumental effects and/or stellar variability and that these effects are greatest for Kepler-7b and Kepler-43b. Furthermore, for Kepler-43b we find a phase function amplitude much larger than the eclipse depth, which is only physically possible if planet does not fully pass behind the star. This would require a highly inclined and eccentric orbit both of which are not seen in the light curve and radial velocity data. Due to the large variations in our bootstrap parameters for Kepler-43b and unphysical phase curve measurements, we conclude that it does not exhibit a planetary phase curve signal.

For seven planets (Kepler-5b, Kepler-6b, Kepler-10b, Kepler-91b, Kepler-412b, KOI-13b and TrES-2b) our analysis did not favour an offset in the peak of their planetary light, while for the other seven (Kepler-7b, Kepler-8b, Kepler-12b, Kepler-41b, Kepler-43b, Kepler-76b and HAT-P-7b) we find both eastward and westward offsets. For the two hottest planets, Kepler-76b and HAT-P-7b, with offsets of 0.023 ± 0.003

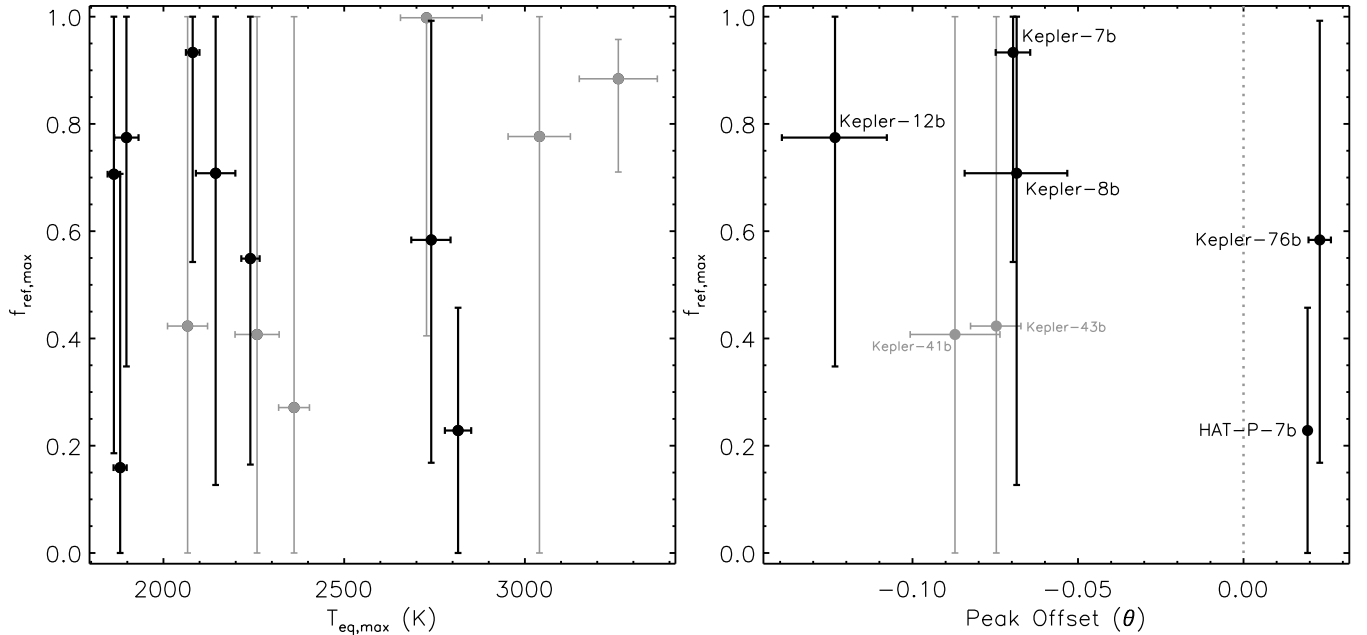


FIG. 8.— Left: Maximum equilibrium temperature vs. the fraction of the planet’s brightness due to reflected light. Right: Peak offset of the planet’s phase function vs. the fraction of the planet’s brightness due to reflected light. The grey points indicate values that are either completely unconstrained, are in doubt due to light curve variability, differ in composition compared to the rest of our sample (Kepler-10b) or are strongly influenced by the chosen stellar parameters (KOI-13b). Dotted grey line indicates the boundary between eastward and westward shifts.

and 0.0194 ± 0.0008 , respectively, we find that the planetary light peaks before the eclipse, corresponding to a peak brightness eastward of the substellar point or on the evening-side of the planet. While for the cooler planets, Kepler-7b, Kepler-8b, Kepler-12b, Kepler-41b and Kepler-43b, with offsets between -0.07 and -0.12, the planetary light peaks after the eclipse (i.e. westward or on the morning-side).

These results have drastically increased the number of *Kepler* planets with detected planetary light offsets and provided the first evidence, in the *Kepler* data, for a correlation between the direction of the peak offset and the planet’s temperature. This correlation could possibly arise if hotter planets are dominated by thermal emission and therefore exhibit a hot spot shifted to the east, as theoretically predicted, whereas

cooler planets are dominated by reflected light and have clouds westward of the substellar point (i.e. on the morning-side), as seen for Kepler-7b. However, with this study alone we are not able to determine whether the planets with peak offsets are seen predominantly in reflected light or thermal emission.

We thank Vincent Van Eylen for insightful discussions. This work was supported by grants from the Natural Sciences and Engineering Research Council (NSERC) of Canada to R.J. L.J.E. is supported in part by an NSERC CGS while E.d.M. received partial support from an Ontario Postdoctoral Fellowship.

REFERENCES

- Adams, E. R., Ciardi, D. R., Dupree, A. K., et al. 2012, *AJ*, 144, 42
Akeson, R. L., Chen, X., Ciardi, D., et al. 2013, *PASP*, 125, 989
Albrecht, S., Winn, J. N., Johnson, J. A., et al. 2012, *ApJ*, 757, 18
Angerhausen, D., DeLarme, E., & Morse, J. A. 2014, *ArXiv e-prints*
Barclay, T., Huber, D., Rowe, J. F., et al. 2012, *ApJ*, 761, 53
Barnes, J. W., Linscott, E., & Shporer, A. 2011, *ApJS*, 197, 10
Batalha, N. M., Borucki, W. J., Bryson, S. T., et al. 2011, *ApJ*, 729, 27
Bergfors, C., Brandner, W., Daemgen, S., et al. 2013, *MNRAS*, 428, 182
Bonavita, M., Chauvin, G., Desidera, S., et al. 2012, *A&A*, 537, A67
Bonavita, M., de Mooij, E. J. W., & Jayawardhana, R. 2013, *PASP*, 125, 849
Bonomo, A. S., Hébrard, G., Santerne, A., et al. 2012, *A&A*, 538, A96
Borucki, W. J., Koch, D., Jenkins, J., et al. 2009, *Science*, 325, 709
Cooper, C. S., & Showman, A. P. 2005, *ApJ*, 629, L45
Coughlin, J. L., & López-Morales, M. 2012, *AJ*, 143, 39
Daemgen, S., Hormuth, F., Brandner, W., et al. 2009, *A&A*, 498, 567
Deleuil, M., Almenara, J.-M., Santerne, A., et al. 2014, *A&A*, 564, A56
Demory, B.-O. 2014, *ArXiv e-prints*
Demory, B.-O., Seager, S., Madhusudhan, N., et al. 2011, *ApJ*, 735, L12
Demory, B.-O., de Wit, J., Lewis, N., et al. 2013, *ApJ*, 776, L25
Désert, J.-M., Charbonneau, D., Fortney, J. J., et al. 2011, *ApJS*, 197, 11
Dunham, E. W., Borucki, W. J., Koch, D. G., et al. 2010, *ApJ*, 713, L136
Esteves, L. J., De Mooij, E. J. W., & Jayawardhana, R. 2013, *ApJ*, 772, 51
Faedi, F., Staley, T., Gómez Maqueo Chew, Y., et al. 2013, *MNRAS*, 433, 2097
Faigler, S., Tal-Or, L., Mazeh, T., Latham, D. W., & Buchhave, L. A. 2013, *ApJ*, 771, 26
Fogtman-Schulz, A., Hinrup, B., Van Eylen, V., et al. 2014, *ApJ*, 781, 67
Fortney, J. J., Lodders, K., Marley, M. S., & Freedman, R. S. 2008a, *ApJ*, 678, 1419

- Fortney, J. J., Marley, M. S., Saumon, D., & Lodders, K. 2008b, *ApJ*, 683, 1104
- Fortney, J. J., Demory, B.-O., Désert, J.-M., et al. 2011, *ApJS*, 197, 9
- Gelman, A., & Rubin, D. B. 1992, *StaSc*, 7, 457
- Hauschildt, P. H., Allard, F., Ferguson, J., Baron, E., & Alexander, D. R. 1999, *ApJ*, 525, 871
- Heintz, W. D. 1978, *Geophysics and Astrophysics Monographs*, 15
- Heng, K., Menou, K., & Phillipps, P. J. 2011, *MNRAS*, 413, 2380
- Huber, D., Silva Aguirre, V., Matthews, J. M., et al. 2013, *ArXiv e-prints*
- Jackson, B. K., Lewis, N. K., Barnes, J. W., et al. 2012, *ApJ*, 751, 112
- Jenkins, J. M., Borucki, W. J., Koch, D. G., et al. 2010, *ApJ*, 724, 1108
- Kipping, D., & Bakos, G. 2011, *ApJ*, 730, 50
- Kipping, D. M., & Spiegel, D. S. 2011, *MNRAS*, 417, L88
- Knutson, H. A., Charbonneau, D., Allen, L. E., et al. 2007, *Nature*, 447, 183
- Koch, D. G., Borucki, W. J., Rowe, J. F., et al. 2010, *ApJ*, 713, L131
- Latham, D. W., Borucki, W. J., Koch, D. G., et al. 2010, *ApJ*, 713, L140
- Liddle, A. R. 2007, *MNRAS*, 377, L74
- Lillo-Box, J., Barrado, D., Moya, A., et al. 2013, *ArXiv e-prints*
- Mandel, K., & Agol, E. 2002, *ApJ*, 580, L171
- Mazeh, T., Nachmani, G., Sokol, G., Faigler, S., & Zucker, S. 2012, *A&A*, 541, A56
- Mislis, D., Heller, R., Schmitt, J. H. M. M., & Hodgkin, S. 2012, *A&A*, 538, A4
- Mislis, D., & Hodgkin, S. 2012, *MNRAS*, 422, 1512
- Morley, C. V., Fortney, J. J., Kempton, E. M.-R., et al. 2013, *ApJ*, 775, 33
- Morris, B. M., Mandell, A. M., & Deming, D. 2013, *ApJ*, 764, L22
- Narita, N., Sato, B., Hirano, T., & Tamura, M. 2009, *PASJ*, 61, L35
- Narita, N., Takahashi, Y. H., Kuzuhara, M., et al. 2012, *PASJ*, 64, L7
- O'Donovan, F. T., Charbonneau, D., Mandushev, G., et al. 2006, *ApJ*, 651, L61
- Pál, A., Bakos, G. Á., Torres, G., et al. 2008, *ApJ*, 680, 1450
- Quintana, E. V., Rowe, J. F., Barclay, T., et al. 2013, *ApJ*, 767, 137
- Rouan, D., Deeg, H. J., Demangeon, O., et al. 2011, *ApJ*, 741, L30
- Sanchis-Ojeda, R., Rappaport, S., Winn, J. N., et al. 2014, *ArXiv e-prints*
- , 2013, *ApJ*, 774, 54
- Santerne, A., Bonomo, A. S., Hébrard, G., et al. 2011, *A&A*, 536, A70
- Showman, A. P., & Polvani, L. M. 2011, *ApJ*, 738, 71
- Shporer, A., Jenkins, J. M., Rowe, J. F., et al. 2011, *AJ*, 142, 195
- Shporer, A., O'Rourke, J. G., Knutson, H. A., et al. 2014, *ArXiv e-prints*
- Sliski, D. H., & Kipping, D. M. 2014, *ArXiv e-prints*
- Sozzetti, A., Torres, G., Charbonneau, D., et al. 2007, *ApJ*, 664, 1190
- Szabó, G. M., Szabó, R., Benkő, J. M., et al. 2011, *ApJ*, 736, L4
- Torres, G., Fischer, D. A., Sozzetti, A., et al. 2012, *ApJ*, 757, 161
- Triaud, A. H. M. J., Queloz, D., Hellier, C., et al. 2011, *A&A*, 531, A24
- Van Eylen, V., Kjeldsen, H., Christensen-Dalsgaard, J., & Aerts, C. 2012, *Astronomische Nachrichten*, 333, 1088
- Van Eylen, V., Lindholm Nielsen, M., Hinrup, B., Tingley, B., & Kjeldsen, H. 2013, *ApJ*, 774, L19
- Welsh, W. F., Orosz, J. A., Seager, S., et al. 2010, *ApJ*, 713, L145
- Winn, J. N., Johnson, J. A., Albrecht, S., et al. 2009, *ApJ*, 703, L99
- Zechmeister, M., & Kürster, M. 2009, *A&A*, 496, 577

APPENDIX

TABLE 1
LITERATURE PHASE CURVE PARAMETERS

Reference	F_{ecl}	A_{p}	A_{e}	A_{d}	Reference	F_{ecl}	A_{p}	A_{e}	A_{d}
KOI-13b					HAT-P-7b				
This work	172.0±1.4	151.9±2.2	74.1^{+5.7}_{-5.1}	10.02^{+0.53}_{-0.48}	This work	71.2±1.5	73.3±2.7	19.0^{+1.7}_{-1.9}	2.22^{+0.17}_{-0.18}
Ang14	162±10 ^e	151±10 ^e	71±10 ^e	0	Ang14	69.3±0.5	60.8±0.5	16.8±0.3	5.3±0.1
Shp14	173.7±1.8 ^e	156.4±2.1 ^f	60.1±1.0	9.45±0.49	Est13	68.31±0.69	65.75±0.48	19.09±0.25	5.80±0.19
Est13	169.6 ^{+2.2} _{-2.3} ^e	143.5 ^{+1.7} _{-1.8} ^e	72.31±0.81 ^e	8.58±0.31 ^e	Mor13	69.1±3.8
Maz12	163.8±3.8	142±3 [†]	66.8±1.6	8.6±1.1	Van12	71.85±0.23	... ^a	18.9±0.3 ^b	...
Mis&Hod12	... ^a	... ^a	... ^c	... ^c	Jac12	61±3	61	... ^c	... ^c
Cou12	124.3 ^{+6.9} _{-7.8}	Mis&Hel12	... ^a	... ^a	15.5 ^d	3.0
Shp11	...	152.2±2.5 ^{e,f}	57.9±1.3 ^e	10.1±0.8 ^e	Cou12	75.0 ^{+9.5} _{-8.1}	63.2 ^{+13.6} _{-12.6}
Sza11	120±10	Wel10	85.8	63.7	18.65 ^d	...
Kepler-7b					TrES-2b				
This work[†]	38.7^{+8.1}_{-8.6}	48±13	1.44^{+0.19}_{-0.18}	0.526±0.043	This work[†]	7.7±1.8	4.1^{+1.1}_{-1.0}	3.21^{+0.43}_{-0.38}	2.246±0.032
Ang14	46.6±3.9	47.8±5.2	0	3.9±4.0	Ang14	10.9±2.2	3.0±0.8	2.9±0.5	2.0±0.2
Dem13	48±3	50±2	0	0	Est13	7.5±1.7	4.77 ^{+0.65} _{-0.63}	3.67±0.33	2.40±0.30
Cou12	53.2 ^{+14.1} _{-13.0}	0	Bar12	6.5 ^{+1.7} _{-1.8}	3.41 ^{+0.53} _{-0.82}	2.79 ^{+0.44} _{-0.62}	3.44 ^{+0.35} _{-0.33}
Dem11	44±5	42±4	0	...	Kip&Spi11	0	6.5±1.9	1.50 ^{+0.92} _{-0.93}	0.22 ^{+0.88} _{-0.87}
Kip&Bak11	47±14	30±17 ^g	Kepler-10b				
Kepler-5b					This work[†]	7.5^{+1.3}_{-1.5}	9.79^{+2.0}_{-1.8}	0.51^{+0.38}_{-0.21}	0.042^{+0.010}_{-0.013}
This work	18.6^{+3.7}_{-3.5}	19.3^{+6.3}_{-5.3}	3.1^{+2.6}_{-2.3}	1.13^{+0.88}_{-0.82}	Dem14	7.4 ^{+1.1} _{-1.0}	0	0	0
Ang14	19.8±3.6	8.3±2.6	3.1±1.4	0	Fog14	9.91±1.01	8.13±0.68	0	0
Est13	18.8±3.7	16.5±2.0	4.7 ^{+1.0} _{-1.1}	0	San14	7.5±1.4
Dés11	21±6	0	Rou11	5.6±2.0	5.6±2.0	0	0
Kip&Bak11	26±17	0	Bat11	5.8±2.5	7.6±2.0	0	0
Kepler-41b					Kepler-6b				
This work[†]	44±12	69⁺¹⁷₋₁₈	5.3^{+1.4}_{-1.2}	1.09±0.14	This work[†]	11.1±4.0	17.2^{+4.6}_{-4.0}	1.80^{+0.18}_{-0.17}	1.036±0.033
Ang14	46.2±8.7	46.3±7.9	2.8±4.3	0	Ang14	11.3±4.2	9.5±2.7	0	1.0±0.9
Qui13	60±11	37.4±6.3	4.5±3.3	0	Est13	8.9±3.8	12.4±2.0	2.7±1.0	0
San11	64 ⁺¹⁰ ₋₁₂	64 ⁺¹⁰ ₋₁₂	0	0	Dés11	22±7	0
Cou12	77±24	0	Kepler-8b				
Kepler-412b					This work[†]	26.0±7.6	24±11	1.86^{+0.55}_{-0.47}	0.80±0.14
This work[†]	53±14	31±14	9.37^{+2.31}_{-0.63}	1.79±0.14	Ang14	16.5±4.4	13.8±3.7	3.7±2.0	0
Ang14	40.2±9.0	17.3±7.4	6.3±3.9	2.7±2.2	Est13	26.2±5.6	25.3 ^{+2.7} _{-2.6}	2.5±1.2	4.0±1.4
Del14	47.4±7.4	28.8±3.2	10.2±2.5	1.81±0.14	Kepler-76b				
Cou12	69 ⁺³¹ ₋₃₀	0	This work[†]	131.6^{+6.1}_{-6.3}	106.9^{+4.3}_{-4.4}	22.1^{+10.2}_{-7.0}	3.45±0.23
Kepler-12b					Ang14	75.6±5.6	101.3±3.6	22.6±1.9	11.4±1.0
This work[†]	20.2±4.7	22.9^{+4.3}_{-4.1}	0.94^{+0.17}_{-0.15}	0.589^{+0.054}_{-0.053}	Fail3	98.9±7.1	112±5.0 [†]	21.5±1.7	15.6±2.2
Ang14	18.7±4.9	16.7±2.6	0	0	Kepler-91b				
For11	31±8	0	This work	47±18	48⁺¹⁸₋₁₉	61⁺²⁷₋₁₉	0.55^{+0.17}_{-0.14}
Kepler-43b					Lil14	0	25±15	60.5 ⁺¹⁶ ₋₁₇ ^d	1.5 ^{+0.5} _{-1.0} ^d
This work	11⁺³²₋₃₁	71±44	18⁺¹⁹₋₁₇	8.7^{+8.5}_{-8.1}	Est13	38.7±8.2	13.1 ^{+5.8} _{-6.0}	45.2 ^{+3.1} _{-2.1}	0
Ang14	17.0±5.3	51.7±3.3	16.9±2.2	0					

Zero values indicate non-detections.

[†] A_{e} and A_{d} derived from radial velocity measurements.

^a A_{g} reported instead of an amplitude.

^b Adjusted by $1/\pi$.

^c M_{p} reported instead of an amplitude.

^d Converted to a semi-amplitude.

^e Corrected by a dilution factor of $1.913±0.019$ (see Section 2.2).

^f Converted to a peak-to-peak amplitude.

^g A_{p} derived from reported F_{ecl} and F_{n} .

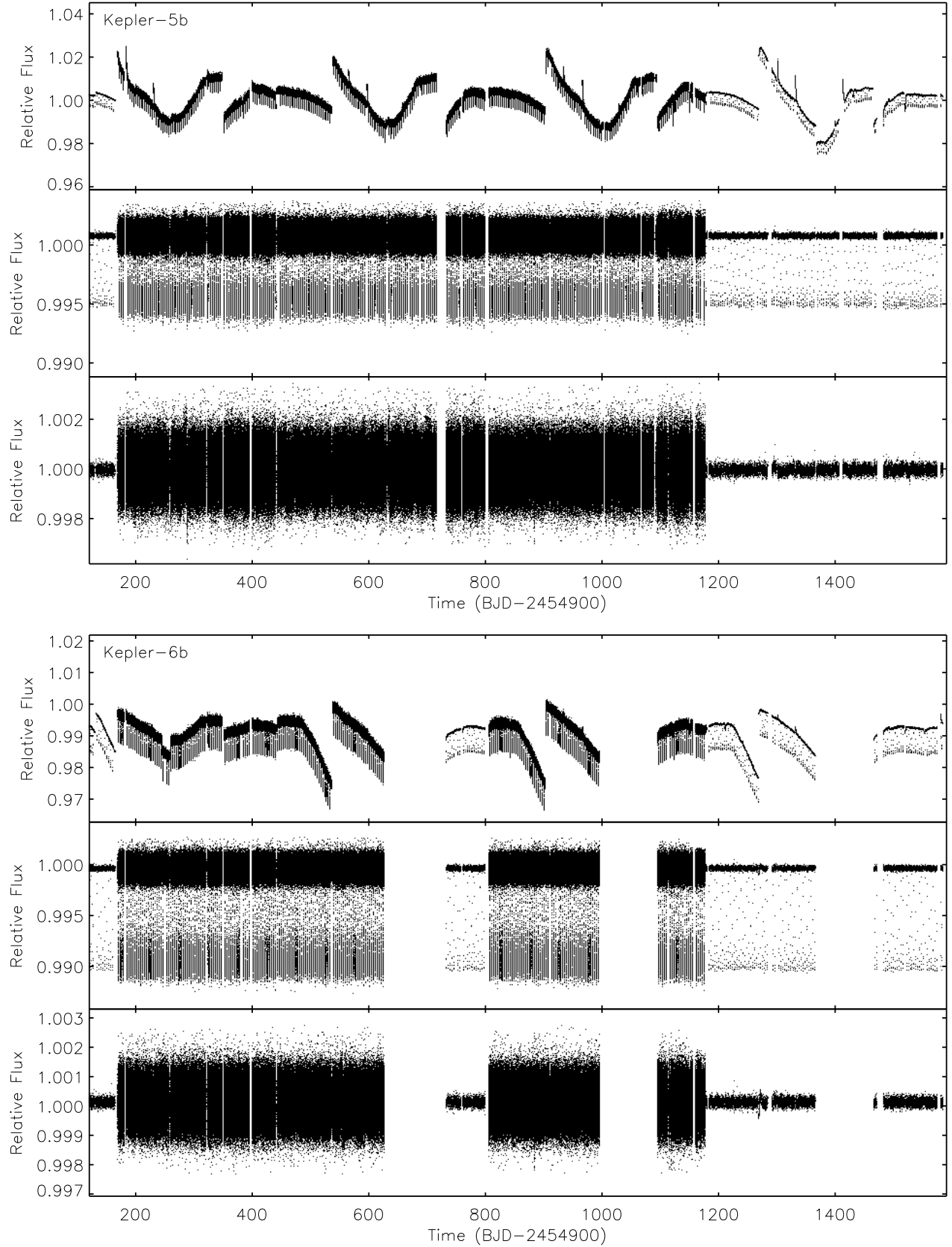


FIG. 1.— For Kepler-5b (top plot) and Kepler-6b (bottom plot), the top panel contains the raw *Kepler* simple aperture photometry light curve, the middle is after cotrending and the bottom is after cotrending and removing the transits and outliers.

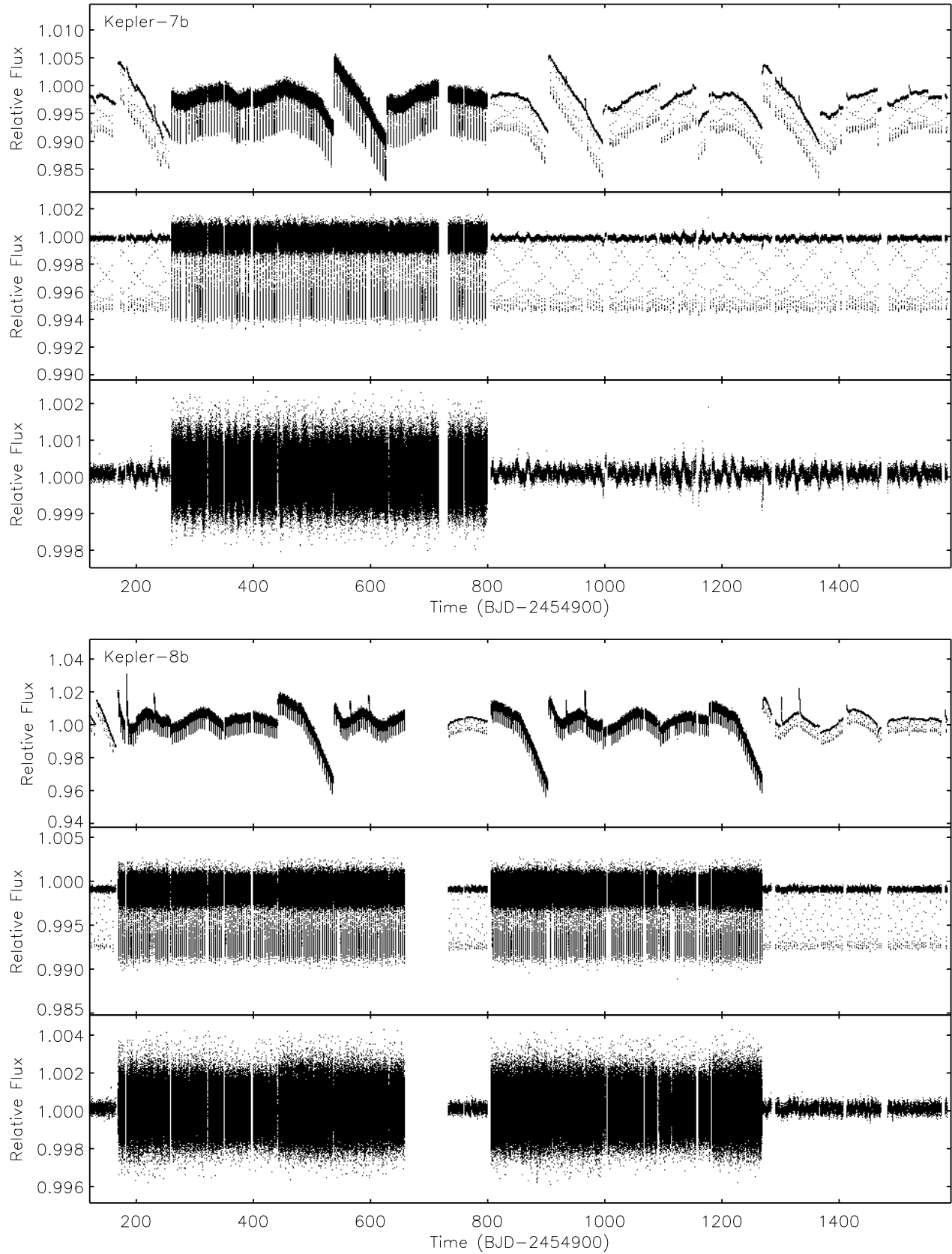


FIG. 2.— Same as Figure 1, but for Kepler-7b (top plot) and Kepler-8b (bottom plot).

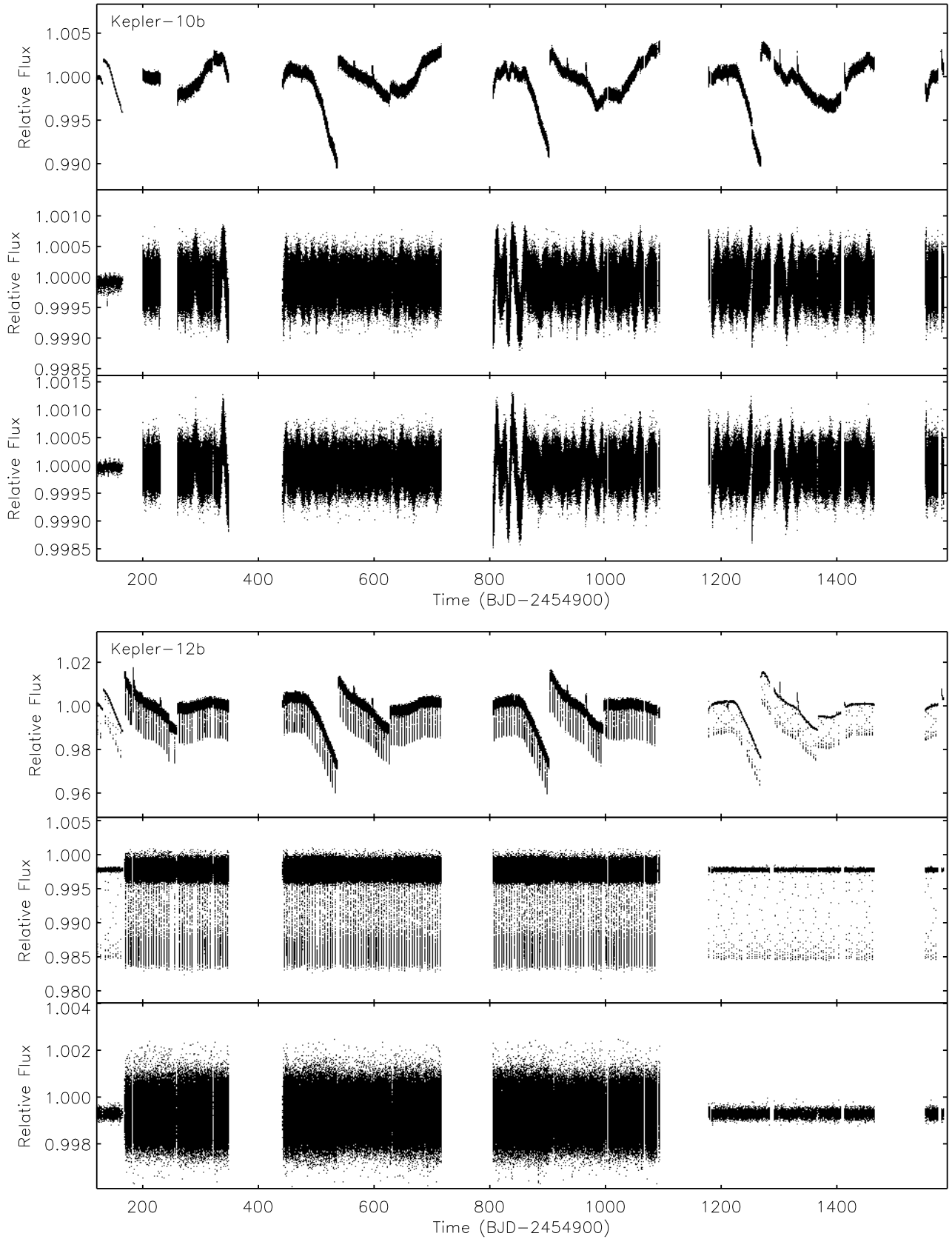


FIG. 3.— Same as Figure 1, but for Kepler-10b (top plot) and Kepler-12b (bottom plot).

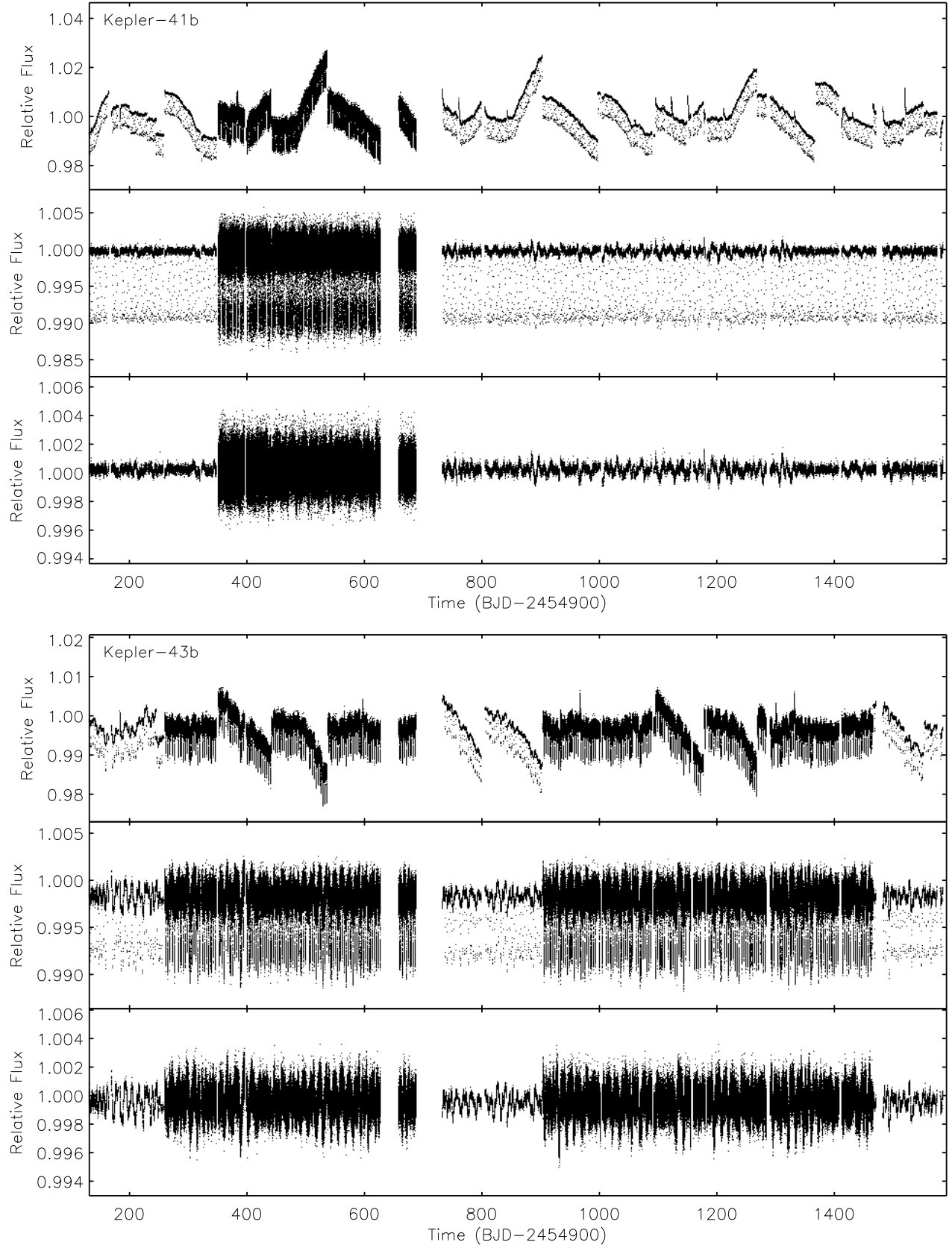


FIG. 4.— Same as Figure 1, but for Kepler-41b (top plot) and Kepler-43b (bottom plot).

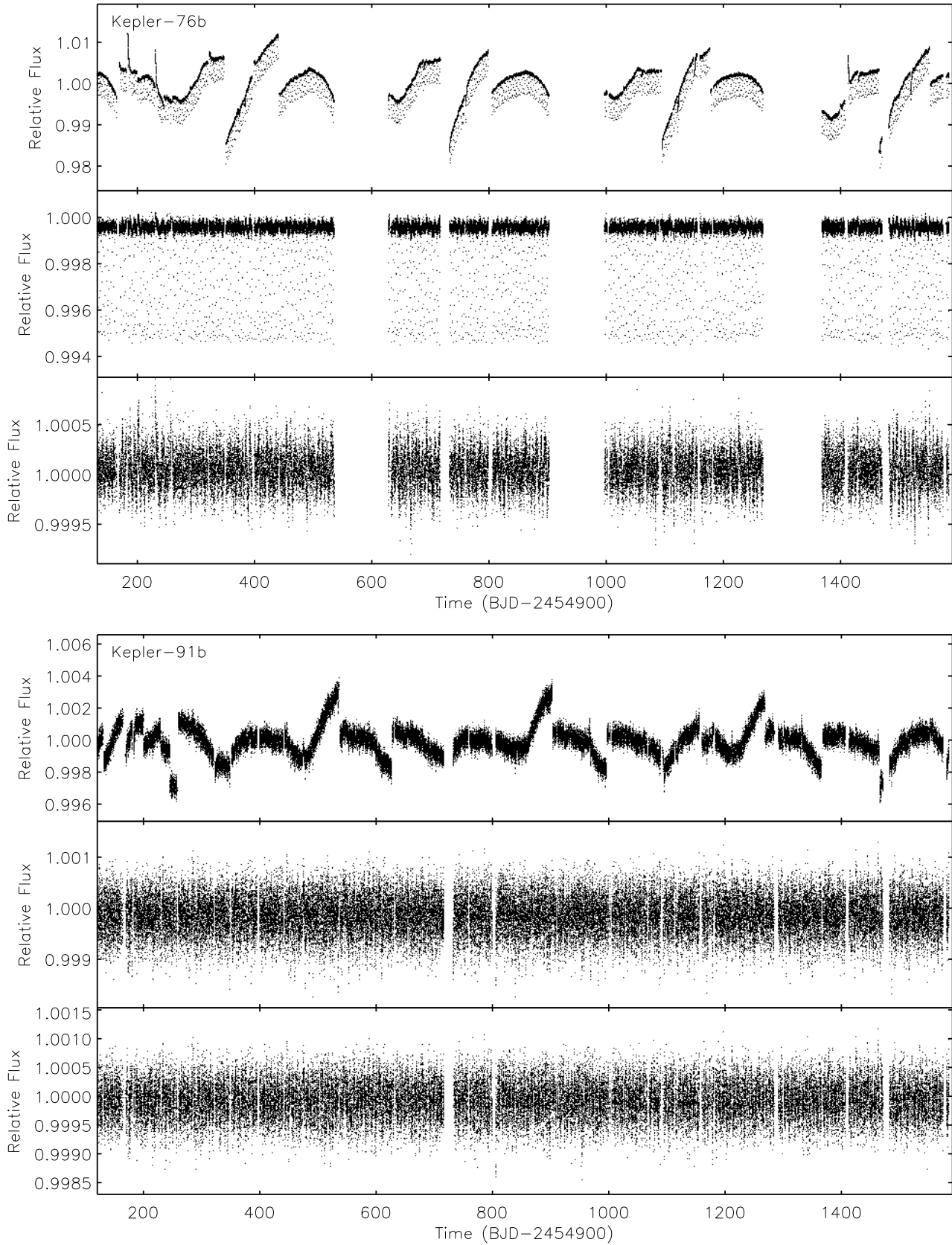


FIG. 5.— Same as Figure 1, but for Kepler-76b (top plot) and Kepler-91b (bottom plot).

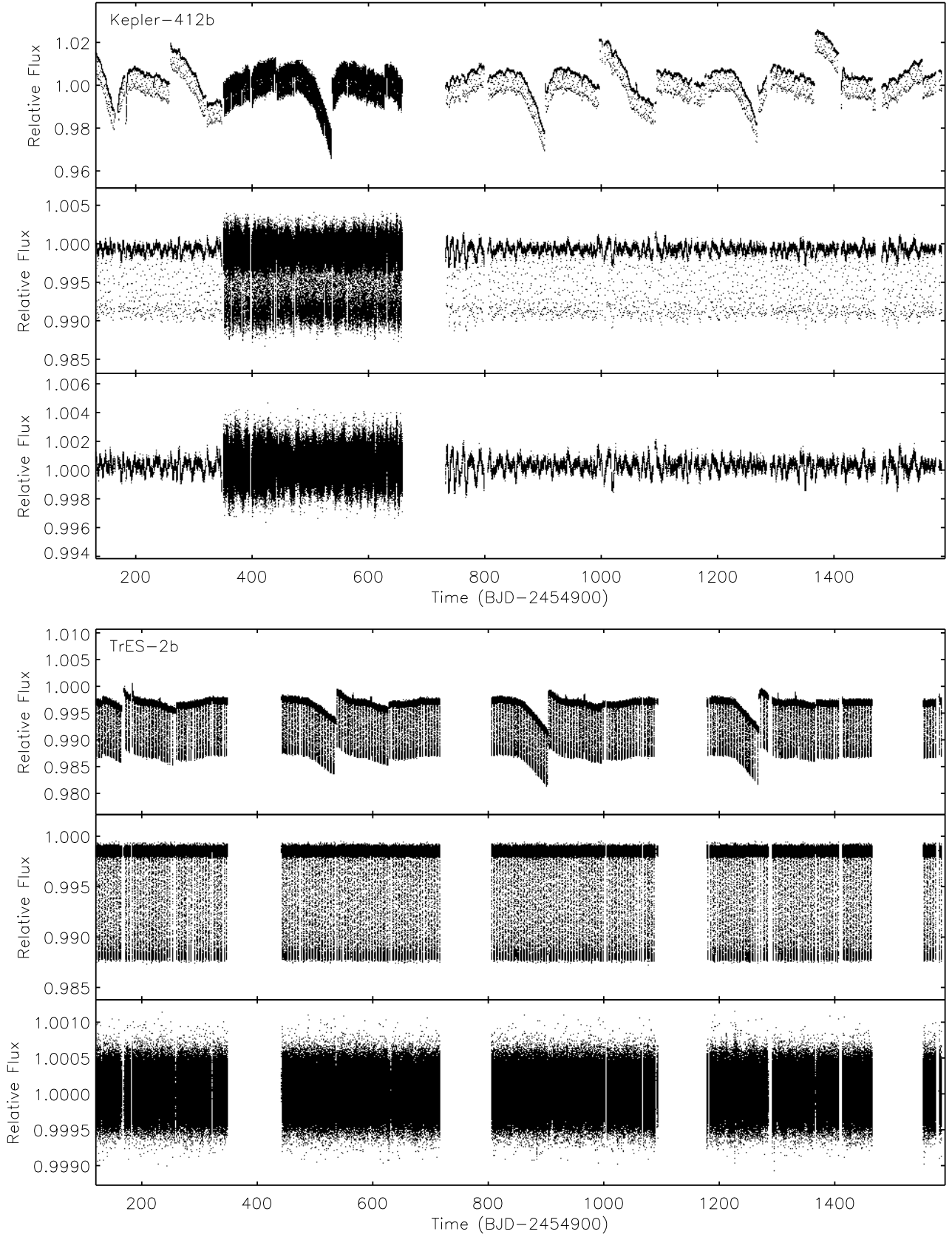


FIG. 6.— Same as Figure 1, but for Kepler-412b (top plot) and TrES-2b (bottom plot).

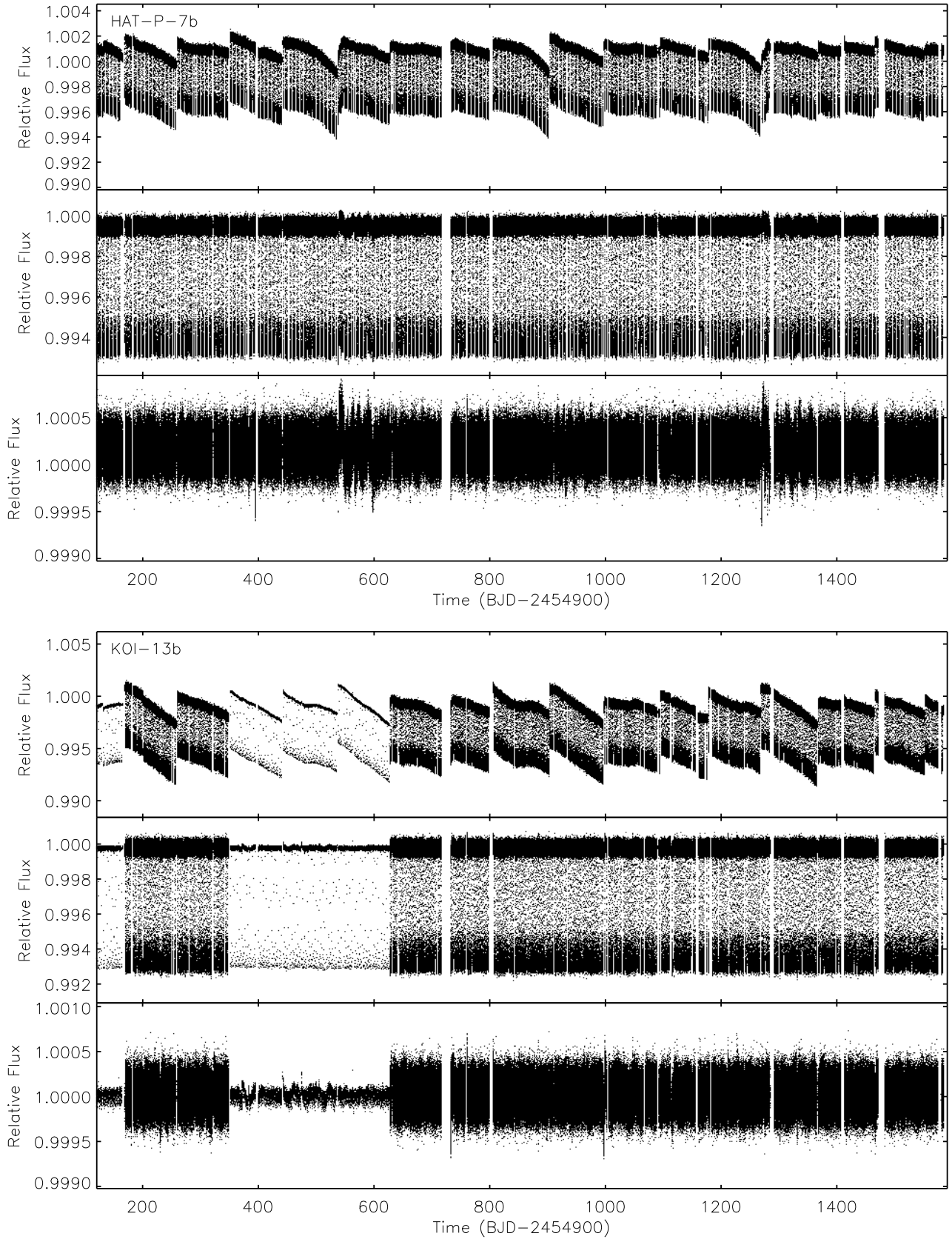


FIG. 7.— Same as Figure 1, but for HAT-P-7b (top plot) and KOI-13b (bottom plot).